Seismotectonic analysis of the 2017 moiyabana earthquake (MW 6.5; Botswana), insights from field investigations, aftershock and InSAR studies

T. Mulabisana, M. Meghraoui, V. Midzi, M. Saleh, O. Ntibinyane, T. Kwadiba, B. Manzunzu, O. Seiphemo, T. Pule, I. Saunders

Seismotectonic Analysis of the 2017 Moiyabana Earthquake (M_W 6.5; Botswana),

Insights from field investigations, aftershock and InSAR studies

Mulabisana, T. [1, 2,5], Meghraoui, M.[1], Midzi, V.[2], Saleh, M.[1,3], Ntibinyane O. [4]
Kwadiba T.[4], Manzunzu, B. [2], Seiphemo O. [4], Pule T.[2], Saunders I.[2]

[1] EOST- ITES, CNRS-UMR 7063, University of Strasbourg, France
[2] Council for Geoscience, 280 Pretoria Street, Silverton, Pretoria, South Africa
[3] NRIAG, Helwan, Egypt
[4] Botswana Geoscience Institute, Lobatse, Botswana
[5] Nelson Mandela University, Port Elizabeth, South Africa

3rd June 2021

Abstract

The 3 April 2017 M_W 6.5, Moiyabana (Botswana) earthquake occurred in the continental interior of the Nubian plate and in a seismogenic region previously considered as stable. Our objective is to combine several approaches (field and remote sensing investigations) in order to adopt a multidisciplinary strategy so as to enhance our understanding of earthquake occurrence in intraplate southern Africa. We analyse the mainshock and aftershocks sequence based on a local seismic network and local seismotectonic characteristics. The earthquake rupture geometry is constrained with more than 900 aftershocks recorded over a period of three months and from the InSAR analysis of Sentinel-1 images (ascending orbit). The mainshock (25.134 E, 22.565 S; depth 22 ± 3 km) was followed by more than 500 events of magnitude $M \geq 0.8$ recorded in April 2017 including the largest aftershock (M_W 4.6 on the 5 April 2017). Focal mechanism solutions of the mainshock and aftershocks display predominance of NW-SE trending and NE dipping normal faulting. Stress inversion of the focal mechanisms produced results that are compatible with a NE-SW extension under normal faulting regime. The InSAR study shows fringes (a pair of ascending images 2017-03-30 and 2017-04-11) with two lobes with 3.86 cm to 5.15 cm coseismic slip on a NW-SE elongated and 40-km-long surface deformation consistent with the mainshock location and normal faulting mechanism. The modelling of surface deformation provides the earthquake rupture dimension at depth with ~ 50 cm maximum slip on a fault plane striking 315°, dipping 45°, -80° rake and with M_o 3.68 x 10^{18} Nm. Although the seismic strain rate is of low level, the occurrence of the 2017 Moiyabana earthquake, followed by an aftershock sequence in the central Limpopo Mobile Belt classifies the intraplate region as an active plate interior.

Keywords: Seismotectonics, Earthquake, Fault, deformation, mainshock, aftershock

48

1 Introduction

50 Continental interiors are often considered as regions of low level of major earthquakes
51 mostly because their earthquake catalogue is limited in time. Amid continental domains,
52 intraplate southern Africa is classified as a Stable Continental Region (SCR) where the build-
53 up of tectonic stresses is slow (e.g., < 8 nanostrain/yr.) and hence considered as among the
54 Earth's least seismic active regions (Stamps et al., 2014; Njoroge et al., 2015; Saria et al.,
55 2014; Johnston, 1996a, 1996b). Although the tectonic and seismicity strain rates are rather
56 low (about 1 nanostrain/yr.) in intraplate southern Africa (the seismotectonic characteristics
57 at the continental scale reveal the existence of active zones crossing the presumably stable
58 African shields (Fig. 1; Hartnady, 1990; Meghraoui et al., 2016). Large earthquakes do occur
59 in areas with no known major historical earthquakes, surface deformation or strain
60 accumulation, but their sources are poorly known. The short record of instrumental and/or
61 historical seismicity of these regions may preclude the full understanding of their
62 seismogenic characteristics and occurrence rate of large earthquakes.

63 The 3 April 2017 Moiyabana earthquake with magnitude M_W 6.5 (Fig. 1) occurred in
64 south-east Botswana, a region which is perceived as a stable continental tectonic domain with
65 apparently no significant evidence of seismic strain release (Fig. 1). The main shock (25.134°
66 E, 22.565° S, 26.5 ± 2.5 km depth according to the Council for Geoscience (CGS), Pretoria;
67 Table 1) and aftershocks are located in a sparsely populated national park. Although the
68 earthquake was widely felt in Botswana, South Africa and Zimbabwe, no severe damage was
69 observed due to the low population density in the epicentral area (Midzi *et al.*, 2018).
70 However, field investigations report slight structural damage with intensity of VI on the
71 Modified Mercalli Intensity scale (MMI-56) observed at about 14 km, 40 km (in a mine) and
72 90 km mainly west of the epicentral location. In addition, Midzi *et al.* (2018) observed N-S

trending clusters of aftershocks recorded during the first month with a spatial and temporal southward migration of seismic events. No strong seismic events have been reported in close proximity to the 2017 Moiyabana earthquake area, except for the 1952 Okavango and 2006 Machaze earthquakes (M_L6.7 and M_W7.0, respectively)

Studies on the earthquake activity of continental interiors have been mainly developed in the eastern United States and the New Madrid seismic zone (Hough and Page, 2011; Calais *et al*., 2016), in eastern Canada (Bent, 1994), in Central Europe (Camelbeeck and Meghraoui, 1998), in intraplate India (Rajendran *et al.*, 1996), in Mongolia (Chéry *et al*., 2001), and in Australia (Crone *et al.*, 1997; Clark *et al.*, 2008). Intraplate deformation can be assessed by the occurrence of strong earthquakes and identification of active tectonic structures in regions far from plate boundaries. The rigidity and stability of the southern Africa shield is questioned following the inferences from seismotectonic and geodetic studies that advocate the existence of incipient rifting south and southwest of the continental East African Rift (Fairhead and Henderson, 1977; Hartnady, 1990; Daly et al., 2020). Although GPS velocities are significantly lower than 1 mm/yr., (Fig. 1; Malservisi *et al.,* 2013; Saria *et al.,* 2014), different authors suggest that there might be a link between the 2017 Moiyabana earthquake sequence and the EARS (Fadel *et al.*, 2020; Chisenga et al., 2020). The invoked reasons are mainly the similarity between the normal faulting mechanism and related extensional tectonic stresses (Fadel *et al.,* 2020), the normal faulting activity of the EARS (e.g., the 22 February 2006 M_W 7.0 Machaze earthquake; Fenton and Bommer, 2006; Saunders et al., 2010) and the Okavango rift basin (e.g., the 11 October 1952 M_W 6.7 earthquake; Modisi *et al.,* 2000; Midzi *et al.,* 2018). Materna *et al.* (2019) imply that the occurrence of the 2017 event on the ancient tectonic zone of the Limpopo Mobile Belt may be responding to the stress field imposed by the EARS (Stamps et al, 2014).

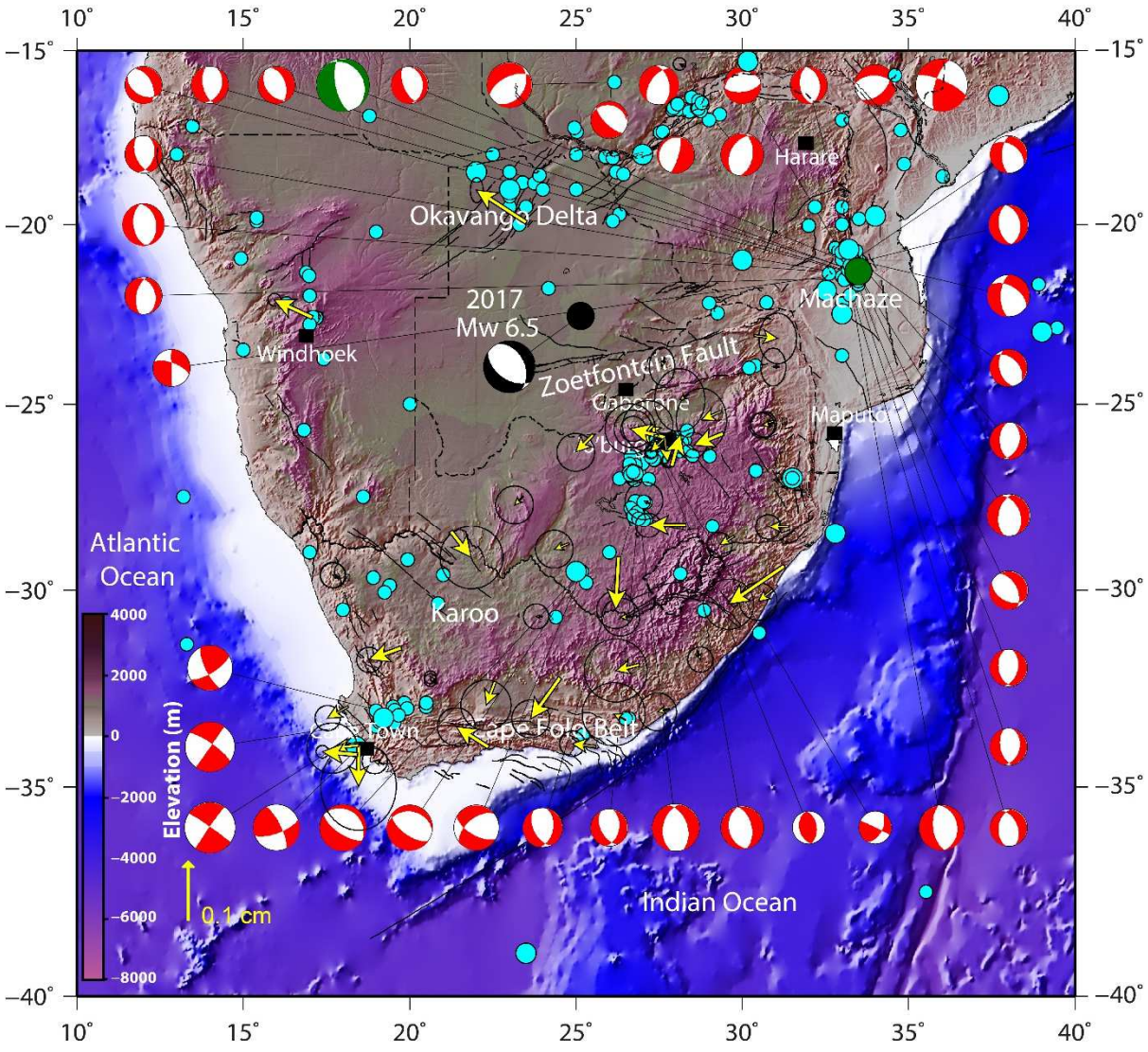

Figure 1: Seismotectonic background of southern Africa (light blue circles and red and white CMT focal mechanism solutions (SM1)), as updated from Meghraoui et al., (2016). Black circle is the location of the 3 April 2017 earthquake and its focal mechanism solution (black and white, CMT-Harvard, https://www.globalcmt.org/CMTsearch.html). The green and white focal mechanism is of the 23 February 2006 Machaze earthquake (Mw 7.0, Mozambique, green circle). GPS velocities (Nubia fixed, yellow arrow with 1σ error ellipse) are from Saria et al. (2014).

Table 1: Source parameters of the 3 April 2017 earthquake from various seismological centres.

Seismological Centre	Long. (°)	Lat. (°)	M_0 (Nm)	M_w	Depth (km)	Strike	Dip	Rake
USGS (Wpha)	25.15	-22.678	6.19×10^{18}	6.5	23.5	343	44	-62
GFZ	25.22	-22.66	6.3×10^{18}	6.5	27	331	37	-73
Geoscope	25.15	-22.678	5.86×10^{18}	6.4	29	333	36	-72
CMT Harvard	25.21	-22.54	7.01×10^{18}	6.5	30	332	41	-70
CGS (Pretoria) Midzi et al. (2018)	25.134	-22.565	-	6.5	26.5 ±2.5	340	46	-61
This study (InSAR)	25.134	-22.565	3.68×10^{18}	6.4	22 ±1.5	315	45	-80

In this paper, our objective is to better understand the earthquake generation processes in the 2017 Moiyabana earthquake area using near-field seismology and active tectonics coupled with remote sensing (geomorphic features and InSAR). Following the presentation of the seismotectonic context and a summary of previous works on the 2017 Moiyabana earthquake, we analyse the mainshock and aftershock sequence using the ~3-month records of portable stations supplemented by the seismograms of the permanent Botswana and South Africa seismic networks. The fault rupture geometry and focal mechanism solutions of the 2017 seismic sequence are determined along with the stress tensor distribution. Our InSAR study (from Sentinel-1 images) of the earthquake area provides the coseismic surface deformation, which coincides with the aftershock distribution and supports the inverse modelling of the fault-rupture parameters. The fault rupture geometry obtained from the seismic sequence and surface deformation is correlated with the composite fault escarpment identified SE of the earthquake area. We finally discuss the driving mechanisms and implications of the intraplate seismic activity and crustal deformation in southern Africa.

2 Seismotectonic setting and previous works

The collision of the Archean Kaapvaal and Zimbabwe Cratons between 2.7 and 2.6 Ga led to the formation of the Limpopo Mobile Belt, which constitute the site of the 2017 Moiyabana earthquake (Roering *et al.*, 1992; Brown *et al.*, 2008; Begg *et al.*, 2009). NW-SE trending shear zones within the Limpopo Mobile Belt are well identified by Bouguer anomalies (Ranganai *et al.*, 2002). The E-W trending Zoetfontein fault zone south of the earthquake location (Fig. 1.) developed in the lower Proterozoic era (Lekula *et al.*, 2018). Fourie *et al.* (2014) modelled the 380 m throw on the eastern part of the Zoetfontein zone and Lekula *et al.* (2018) attributed the western part to a 200 m graben structure. The crustal structure beneath cratons obtained from receiver functions and broadband seismic stations characterize the Moho average depth at 38 km, which is considered as the thinnest crust in the region (Nguuri *et al.*, 2001) and may explain the ~30 km thickness of the seismogenic layer (Midzi *et al.*, 2018).

The occurrence of the 2017 Moiyabana, Botswana earthquake prompted several works on its origin, driving mechanism, stress distribution and seismic strain accumulation. Kolawole *et al.* (2017) used high-resolution aeromagnetic, gravity data and InSAR analysis, and inverse modelling to investigate the Precambrian basement lithospheric structures and concluded that the fault rupture follows a distinct NW striking and NE dipping magnetic lineament within the Precambrian basement. Albano *et al.* (2017) show a model of the coseismic fault from InSAR results and infer a 20- km-long rupture plane, dipping 65° to the northeast, with a right-lateral component, and 2.7 m maximum slip at depth.

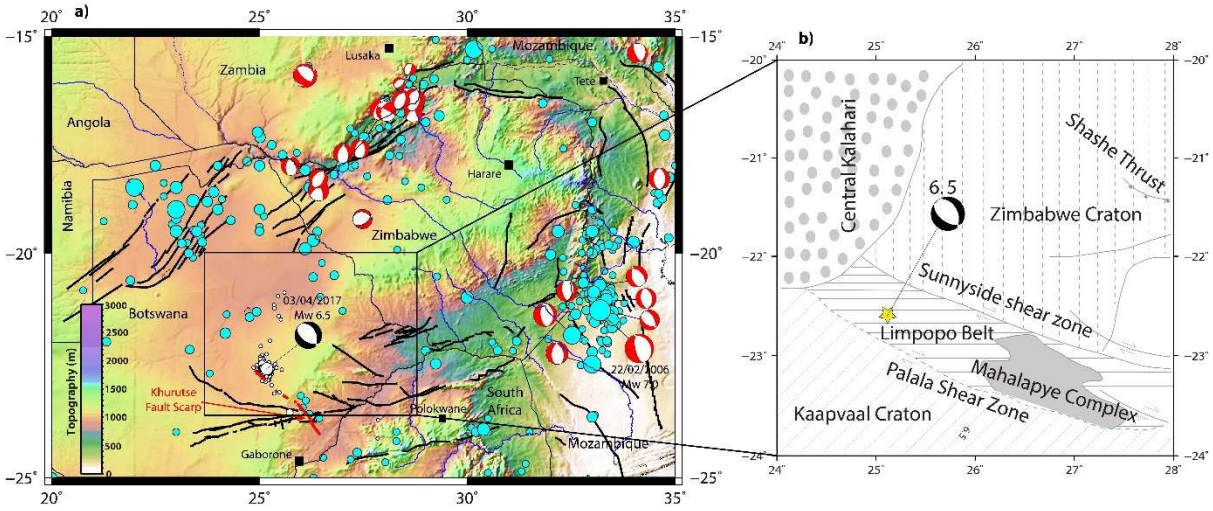

Figure 2. ***a)*** *Seismotectonic framework excerpt of the Seismotectonic Map of Africa (modified from Meghraoui et al., 2016) with focal mechanism (CMT-Harvard) of the 2017 Moiyabana mainshock. The red line is the inferred Khurutse fault scarp, cyan circles are background seismicity with magnitude* $4.5 \leq M \leq 7.5$; ***b)*** *Structural geology background of the 2017 earthquake area (modified from Brown et al., 2008). The mainshock is indicated by a yellow star.*

Gardonio *et al.* (2018) provide a seismicity study coupled with InSAR results to infer 6 cm of subsidence, 10 km along the dip and 30 km along the strike of the fault and suggest that the pore fluids pressure from a deep source at 29 ± 4 km might be the cause of the 2017 event. Moorkamp *et al.* (2019) investigated the epicentral area with seismic velocity and resistivity profiles and showed the collocation of a weak upper mantle and weak crustal structure between strong Precambrian blocks. They also show that although the modelled resistivity may indicate fluid activation on conductive structures, there is no evidence of the fluid migrating upward or a tectonic structure presenting to be the source of the 2017 Moiyabana earthquake within the vicinity. Fadel *et al.* (2020) suggest a link with the EARS by modelling the 3D crustal and upper mantle shear wave velocity structure of Botswana and concluded that the rift can be the source of a fluid driven from ~150 km depth of the north-eastern tip of Botswana to migrate to the edge of the Kaapvaal Craton and the earthquake

area. Chisenga et al. (2020) modelled the Bouguer gravity and produced a high-resolution crustal thickness map of Botswana which suggests a correlation of the earthquake activity with the thermal fluid and elevated heat flow from EARS. Thomas (2020) also used the analysis of Sentinel images and provided an interferogram that suggests 9 to 10 cm total coseismic slip at the surface. Finally, Olebetse *et al.* (2020) studied foreshock and aftershock events recorded by the Botswana seismic network and suggest a correlation with local geological structures of the Kaapvaal Craton and Limpopo mobile belt. Although no field investigations were conducted after the mainshock, most studies correlate the 2017 seismic sequence with the tectonic reactivation in the Limpopo Mobile Belt due to thermal fluids and elevated heat flow linked to the EARS.

3 Mainshock and Aftershock Analysis

The mainshock of 3 April 2017 with M_W 6.5 was reported by several international seismological centres (Table 1) but the South African National Seismograph Network (SANSN) provided the most accurate location, as their seismic stations are in close proximity to the source. The epicentre location of the SANSN (Council for Geoscience, Pretoria) also includes data from the Botswana seismic network (Fig. 3). The largest aftershock with magnitude M_W 4.6 occurred west of the mainshock on 5 April 2017 at a much shallower depth (~10 km) than the mainshock.

Following the mainshock, an aftershock sequence was recorded from 8 April to 29 June 2017 by a temporary network and shows more than 900 earthquake records. Aftershocks that occurred prior to 8 April 2017 (i.e., date of installation of the temporary network as presented in Figure 3) and recorded by the Council for Geoscience (CGS) together with the Botswana Geological Institute (BGI) are excluded in our initial seismic sequence analysis (Figs. 5 a and b) due to fixed depth values (see figure in SM2). This early aftershocks-sequence consists of

65 events reaching M_L4.1 with a fixed constant 5-km-depth. The fixing of earthquake depths by the CGS is done in their routine seismic data analysis, as the sparse nature of the network makes it difficult to confidently determine depth values. The record of the seismic sequence (that benefited from the collaboration between seismic networks of the CGS and the BGI) includes seismic events with magnitude as low as M_L 0.8 with a decrease of daily occurrence rate from 101 to 20 seismic events within the first month of record (Midzi *et al.*, 2018). Following the mainshock, the seismicity decay obtained from the daily number of aftershocks conforms to the Omori's law (Fig. 4; Utsu et al., 1995).

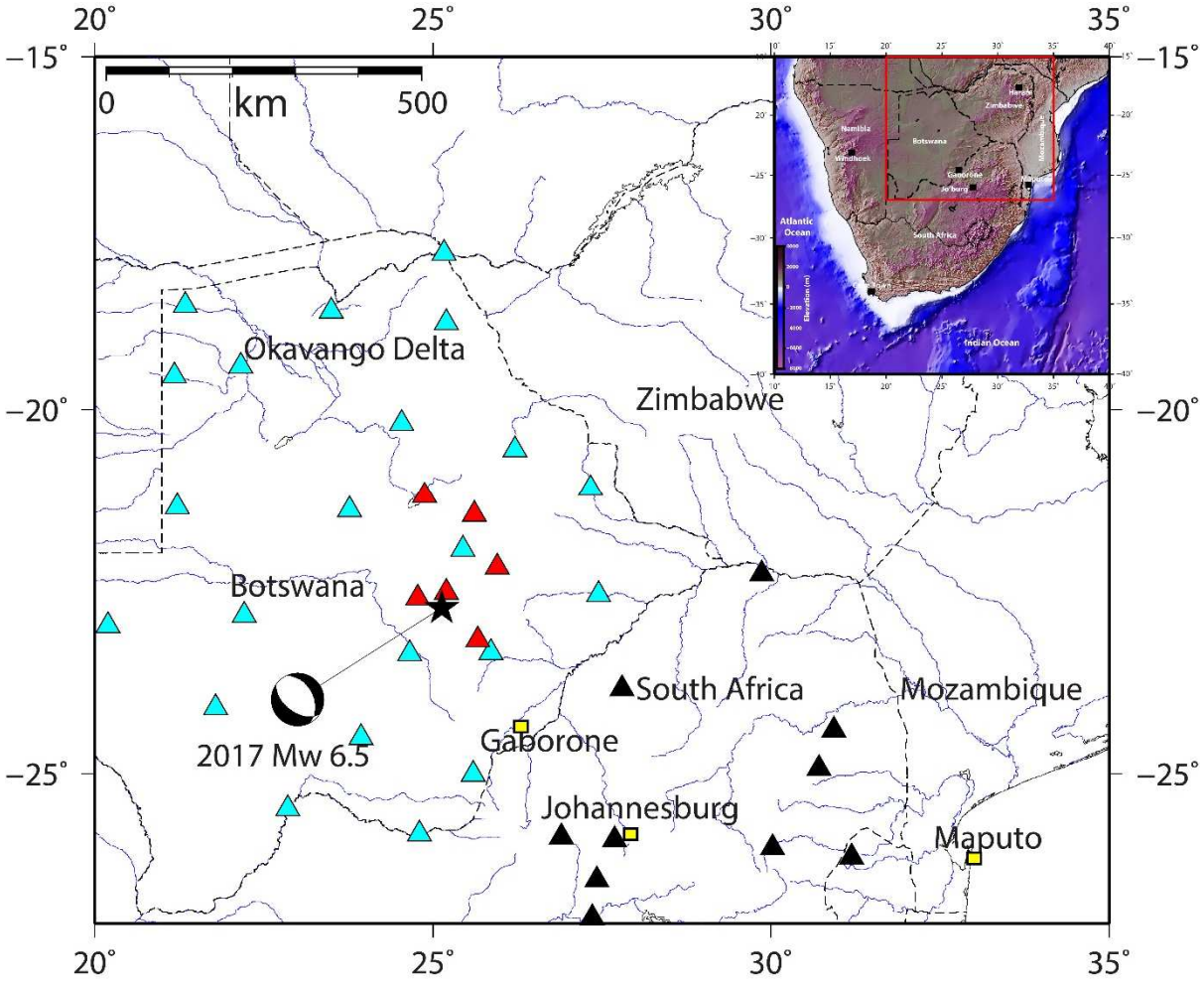

Figure 3. Seismic stations which recorded the mainshock (black star) and aftershocks. Focal mechanism is from Harvard CMT. The seismic stations in cyan triangles are managed by

Botswana Geoscience Institute and black triangles by Council for Geoscience. Portable seismic stations (red triangles) were temporarily installed and recorded aftershocks from the 8th of April to the 29th of June 2017. The inset image shows the location of Figure 3 in red square.

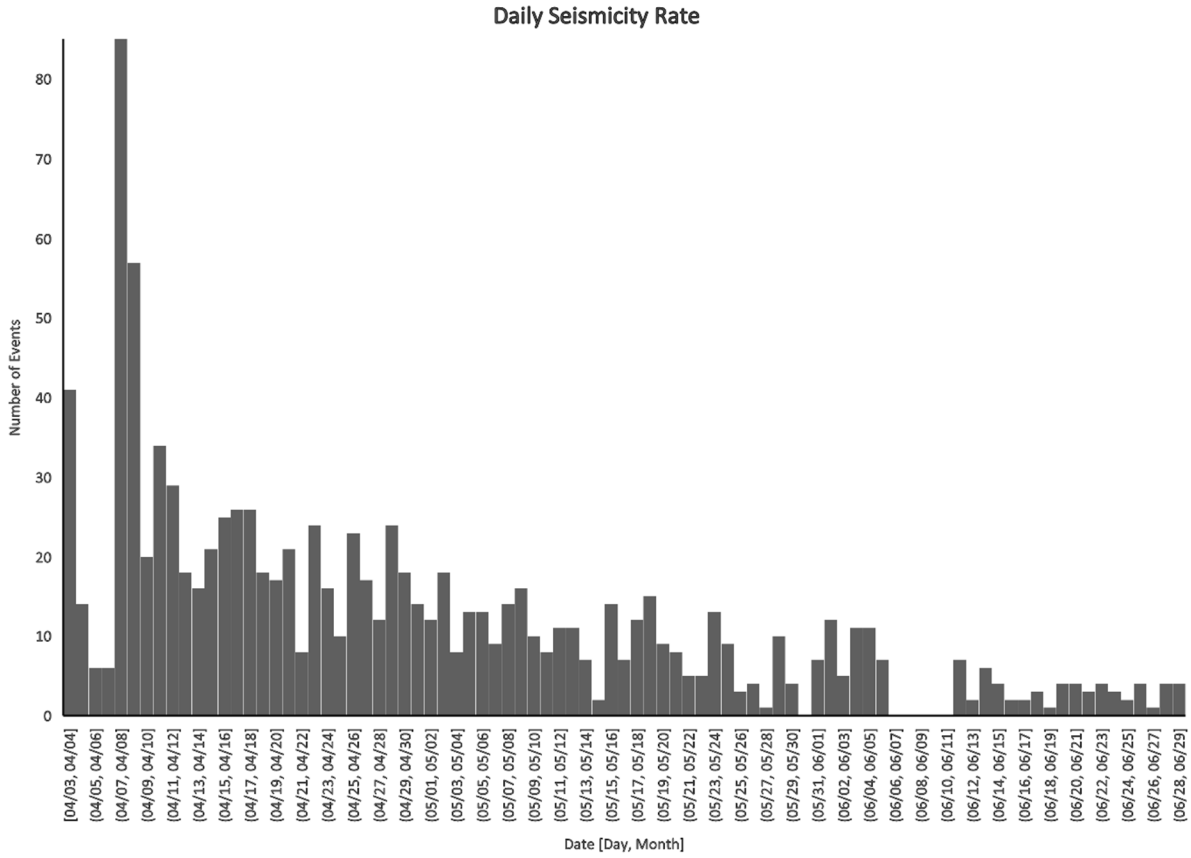

Figure 4. Daily number of seismicity recorded from the 3rd of April to the 29th of June 2017.

The initial earthquake locations were obtained using the modified HYPOCENTER program (Lienert *et al.,* 1986; Lienert and Havskov, 1995) in the SEISAN software package (Ottemöller *et al.,* 2018). This method utilises the interactive, least squares method to determine the location of the earthquake. The three-layer velocity model developed for South Africa (Midzi et al., 2010) was used in the location process (Table 2) resulting, on average, with epicentral and depth uncertainty of 1.5 km and 2.5 km, respectively.

Table 2: Velocity model used in aftershock locations (Midzi et al., 2010).

Modified depth to top of layer (km)	P-wave velocity (km/s)
0.00	5.80
20.00	6.50
38.00	8.04

The initial location of seismic sequence shows two clusters with a NNW-SSE trending western dense aftershock distribution and a N-S trending but sparse eastern aftershock sequence (Fig. 5a). The western aftershocks cluster includes the mainshock and largest aftershock whilst the eastern aftershock sequence, which is located about 20 km further east, includes one of the largest aftershocks with a magnitude M_L 4.2. The depth cross-section of the aftershocks shows the two clusters with a depth distribution of seismic events between 7 and 30 km for the western sequence, and between 4 and 12 km for the eastern aftershocks (Fig. 5b). The aftershocks also show a significant temporal eastern migration with the occurrence of the eastern seismic sequence mostly in June 2017 (Fig 6a). Fig. 6b illustrates the frequency of aftershocks versus the magnitude within the three months when temporary stations were deployed. The activity rate and b-value are 3.8 and 0.78, respectively, and we note the gap of earthquake magnitude between 4.6 and 6.5, implying that the M_W 6.5 event is a characteristic earthquake.

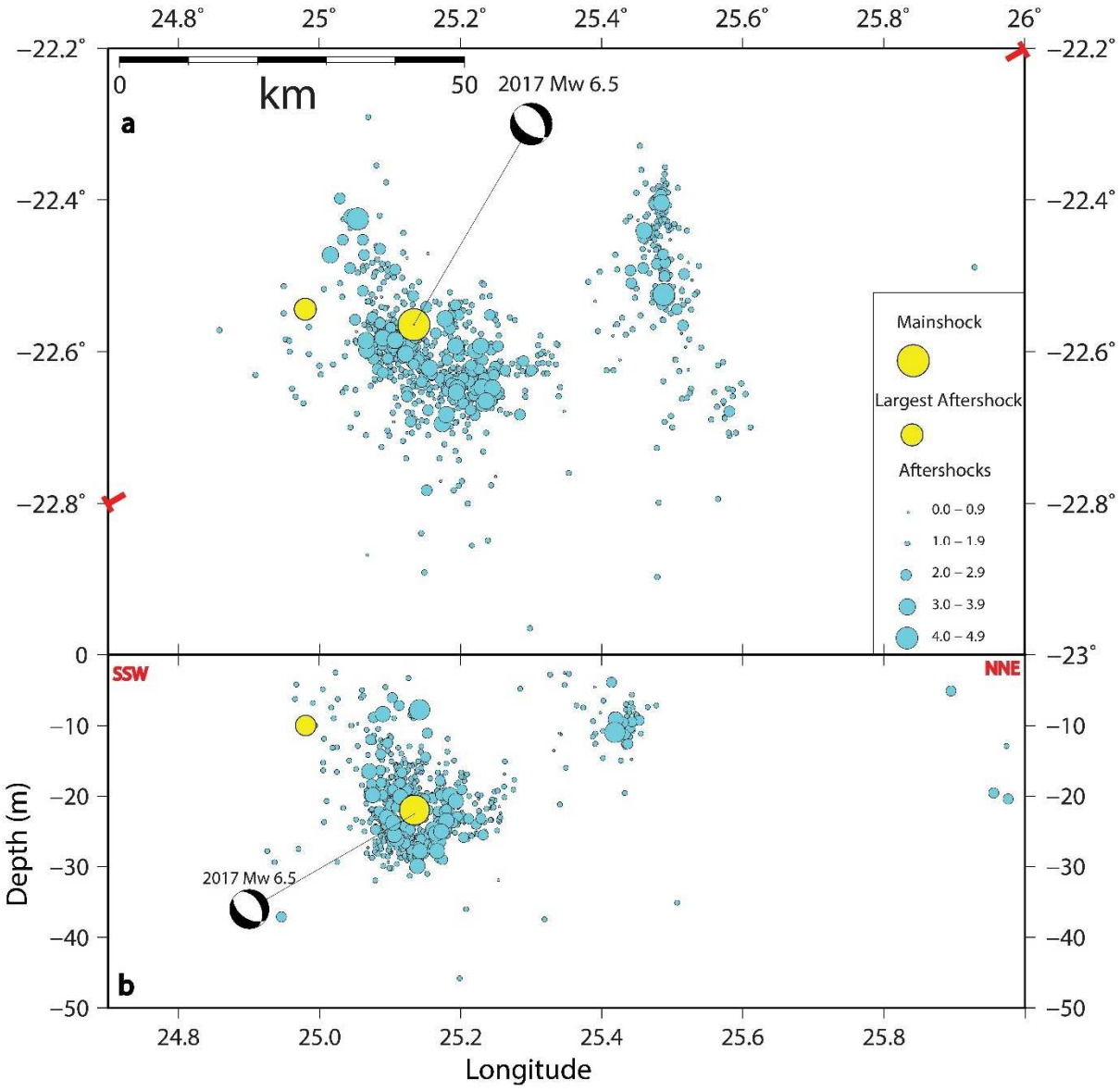

Figure 5. ***a)*** *Mainshock and the initial aftershocks sequence location of the 2017 Moiyabana earthquake with CMT-Harvard focal mechanism.* ***b)*** *Cross-section of the 2017 seismic sequence, as indicated by the T-symbols in Fig. 5(a), recorded by temporary network from 8 April to 29 June 2017 (cyan circles) following the mainshock.*

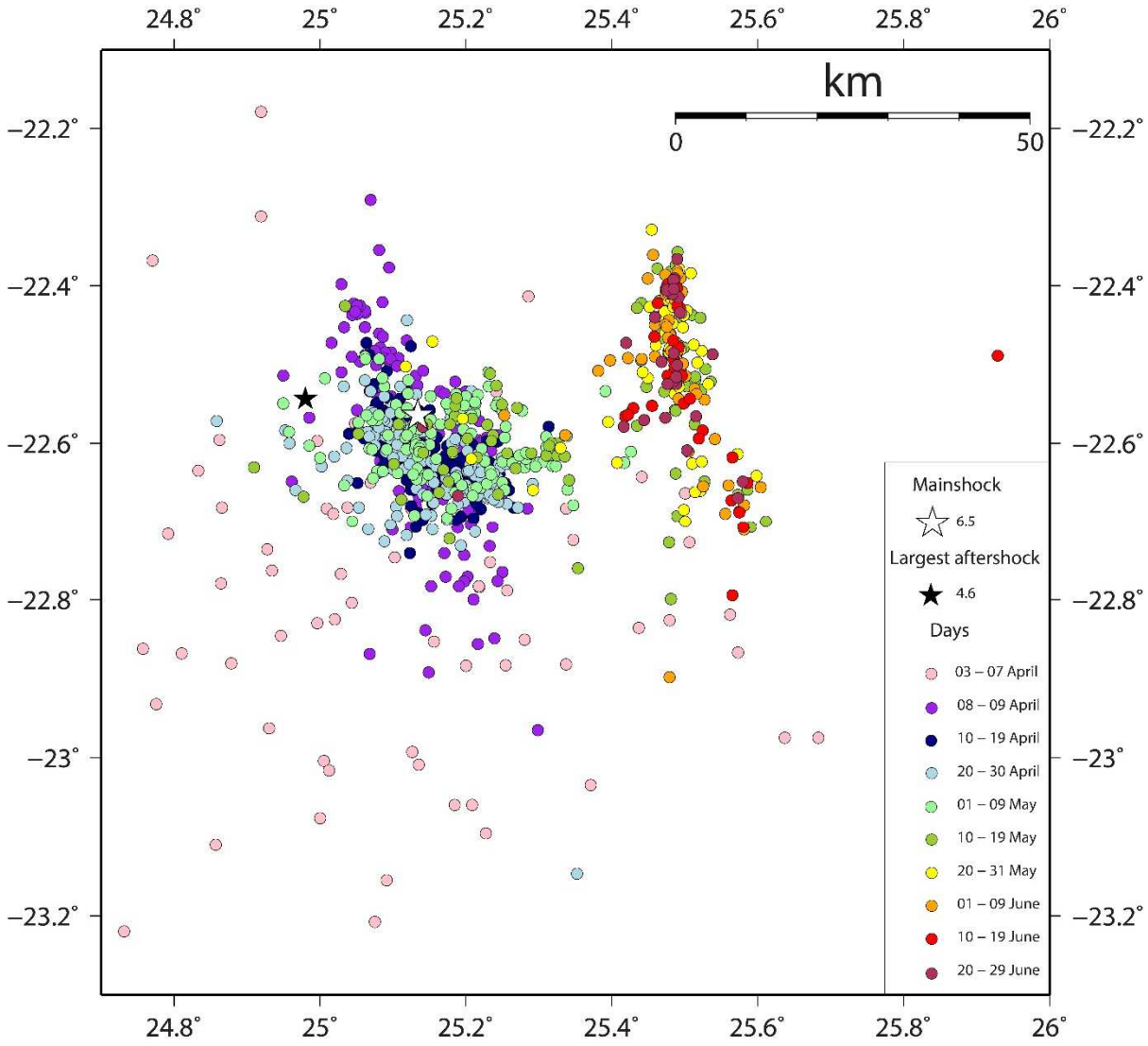

Figure 6. ***a)*** *Migration of more than 900 aftershocks (colour scale) recorded using the temporary network installed from 8 April to 29 June 2017 and 67 aftershocks (pink circles) recorded from 3 to 7 April 2017 by permanent stations. The eastern sequence occurred mostly in June 2017.*

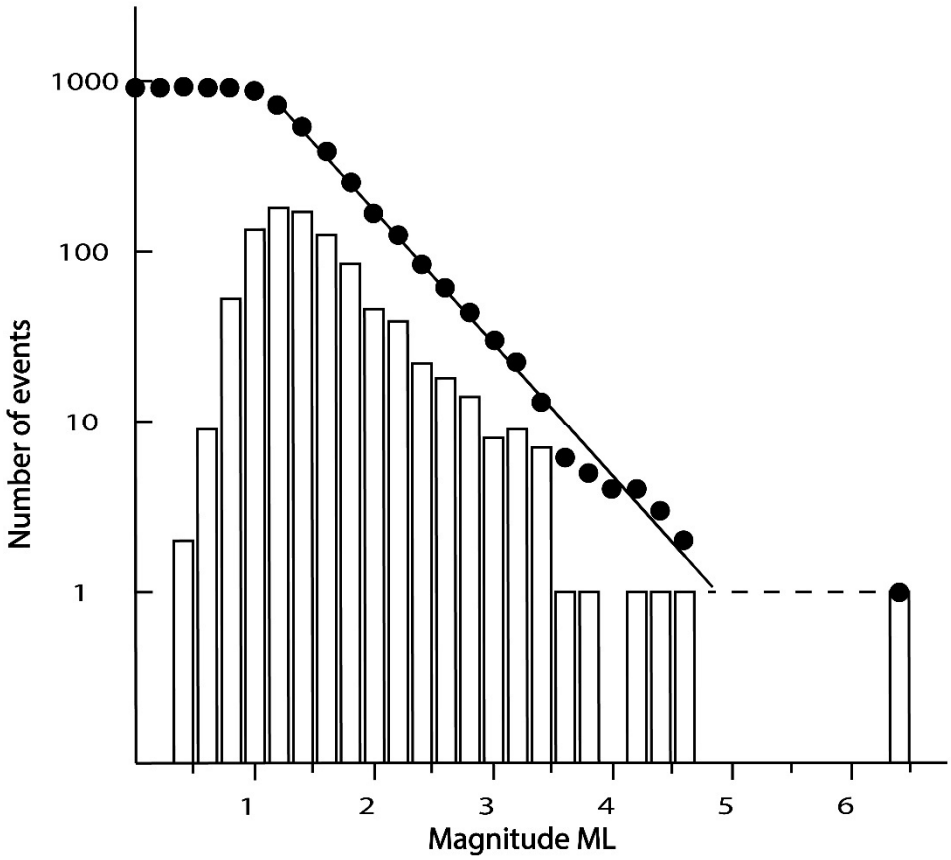

245

246 *Figure 6.* ***b)*** *Gutenberg-Richer relation Log N = 3.8-0.78M_L as applied to the 2017*

247 *earthquake sequence.*

248

249 In order to provide a complete description of aftershock distribution and improve their
250 location and depth, the earthquakes were relocated using a double difference approach as
251 implemented in the HypoDD program (Waldhauser and Ellsworth, 2000). In this seismicity
252 analysis, we do not include aftershocks that occurred prior to the 8 April 2017 due to the
253 distant location (> 150km) of seismic stations. The double difference approach uses cross-
254 correlation between earthquake pairs to extract differential travel times from seismic stations.
255 The cross correlation needs to occur from at least two seismic stations to further constraint
256 the earthquake location. When a seismic station is not part of a pair, it does not contribute to
257 further constrain the seismic source location. The computation reduces random noise in data

by suppressing strong signatures of station geometry and allows a better location of the seismic source.

The HypoDD subprogram ***ph2dt*** is used to process first the seismic events into pairs, minimizing the RMS residuals between the observed and calculated travel time differences of P and S waves at same stations. 699 out of over 900 aftershocks were selected to be relocated considering the quality readings of P and S seismic waves, resulting in 1398 travel times. In this approach, we also consider the velocity model of Table 2, Vp/Vs ratio of 1.74. The aftershock analysis is made within the 50 km distance of the seismic sequence and at a maximum 170 km station distance, while previous studies of Midzi et al. (2010) provide the P-wave velocity 1-D model. The relocated earthquakes shown in Figs 7a and b are obtained from the double difference approach as implemented in the HypoDD program (Waldhauser and Ellsworth, 2000). The stability of the relocated solutions is satisfactory because six portable seismic stations are close to or within the aftershock sequence area and the P and S wave arrivals times allowed for an average 8500 iterations. Following the relocation process, the aftershocks distribution clearly shows the accurate concentration of seismic events in the seismogenic layer and upper crust (see figure in SM3). After relocation, most of the seismicity is located between 8 and 32 km depth, with most of arrival time RMS between 0.1 and 0.3 seconds (Fig. 7c). Taking into account the velocity model of Table 1, the depth uncertainties range between 0.7 and 2.1 km.

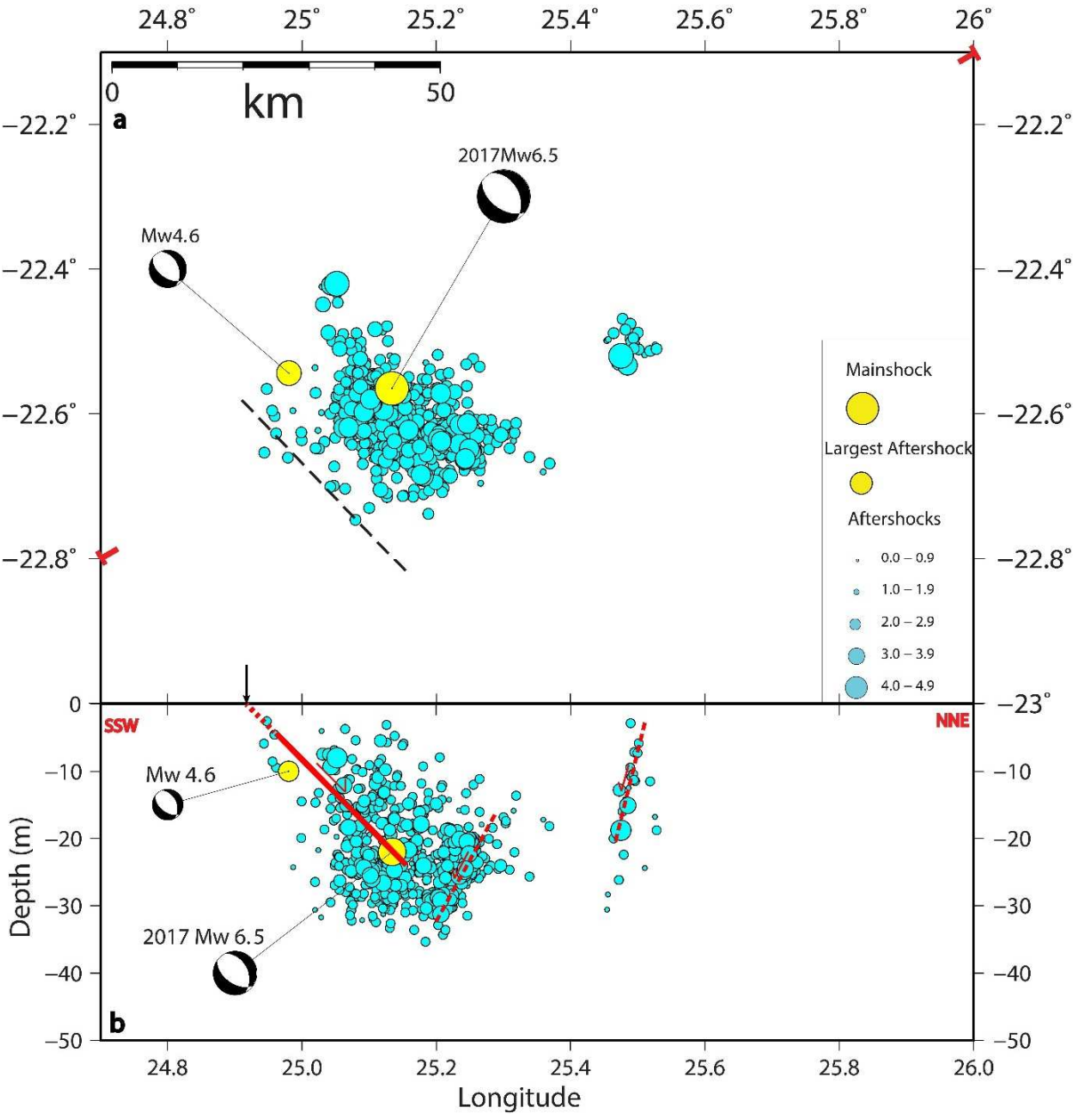

Figure 7. ***a)*** *Spatial distribution of aftershock locations obtained after relocation. Focal mechanism solutions of the mainshock and main aftershock are from CMT Harvard. The dashed line is the coseismic rupture tip inferred from the aftershocks at depth (Fig. 7b) and the analysis of InSAR fringes of coseismic surface deformation (see section on InSAR analysis).* ***b)*** *Aftershock sequence cross-section, as indicated by the T-symbols in Fig. 7(a), after relocation. Focal Red lines are the blind coseismic ruptures inferred from the*

mainshock and aftershocks sequence; the black arrow locates InSAR fringes of coseismic surface deformation (see section on InSAR analysis).

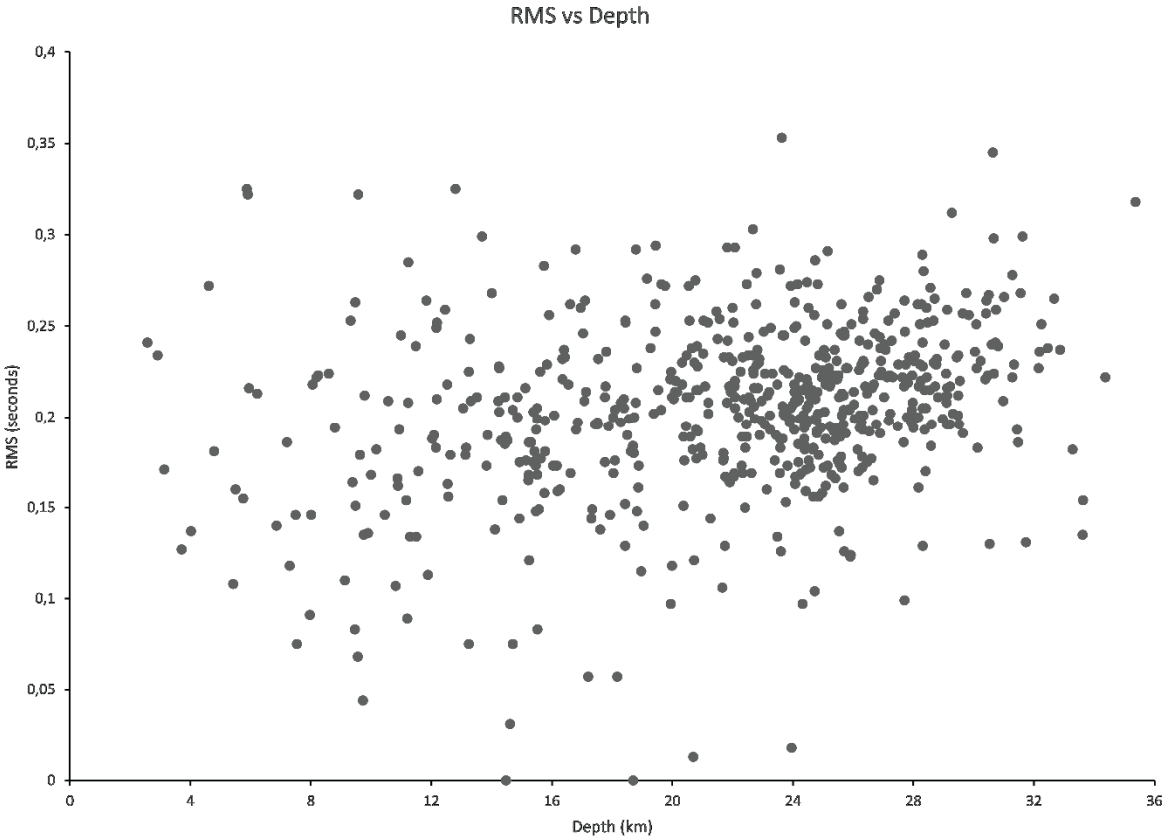

Figure 7. ***c)*** *RMS versus depth after relocating the aftershock sequence.*

Relocated events better show the clustering at depth (Fig. 7b). In the cross-section of Fig. 7(b), the western sequence of aftershocks shows sub-clusters between 10 and 30 km depth suggesting two conjugated fault ruptures. The eastern seismic cluster sequence appears at shallower depths (mostly between 5 and 15 km) and more clustered than in the SEISAN locations. They are well aligned marking a high angle west dipping rupture plane (Fig. 7b). The aftershock distribution and geometry of the inferred fault-ruptures at depth imply a graben-like tectonic structure within this part of the Limpopo Mobile Belt.

299 # 4 Focal Mechanism and Stress Inversion

300 The 2017 mainshock ruptured along a buried fault, which was not previously mapped.
301 Therefore, any information on source geometry and stress orientation in the epicentral area is
302 vital in understanding the driving mechanism. Focal mechanism solutions were calculated to
303 indicate the maximum compressive horizontal and vertical stresses (Zoback and Zoback,
304 1989; Delvaux, 1993; Manzunzu *et al.*, 2017). The focal mechanism solutions for 46 selected
305 aftershocks were computed based on first-motion polarities of P-wave (Ross *et al.*, 2018),
306 using FOCMEC module in the SEISAN software package (Ottemöller et al., 2018). The
307 degree of search varies from 2 to 20 degrees for different aftershocks. The focal mechanism
308 solutions are shown in Fig. 8 and parameters are listed in SM4. The selected seismic events
309 were those with signal to noise ratio above 2.0 and recorded by at least 5 stations with clear
310 polarity readings.

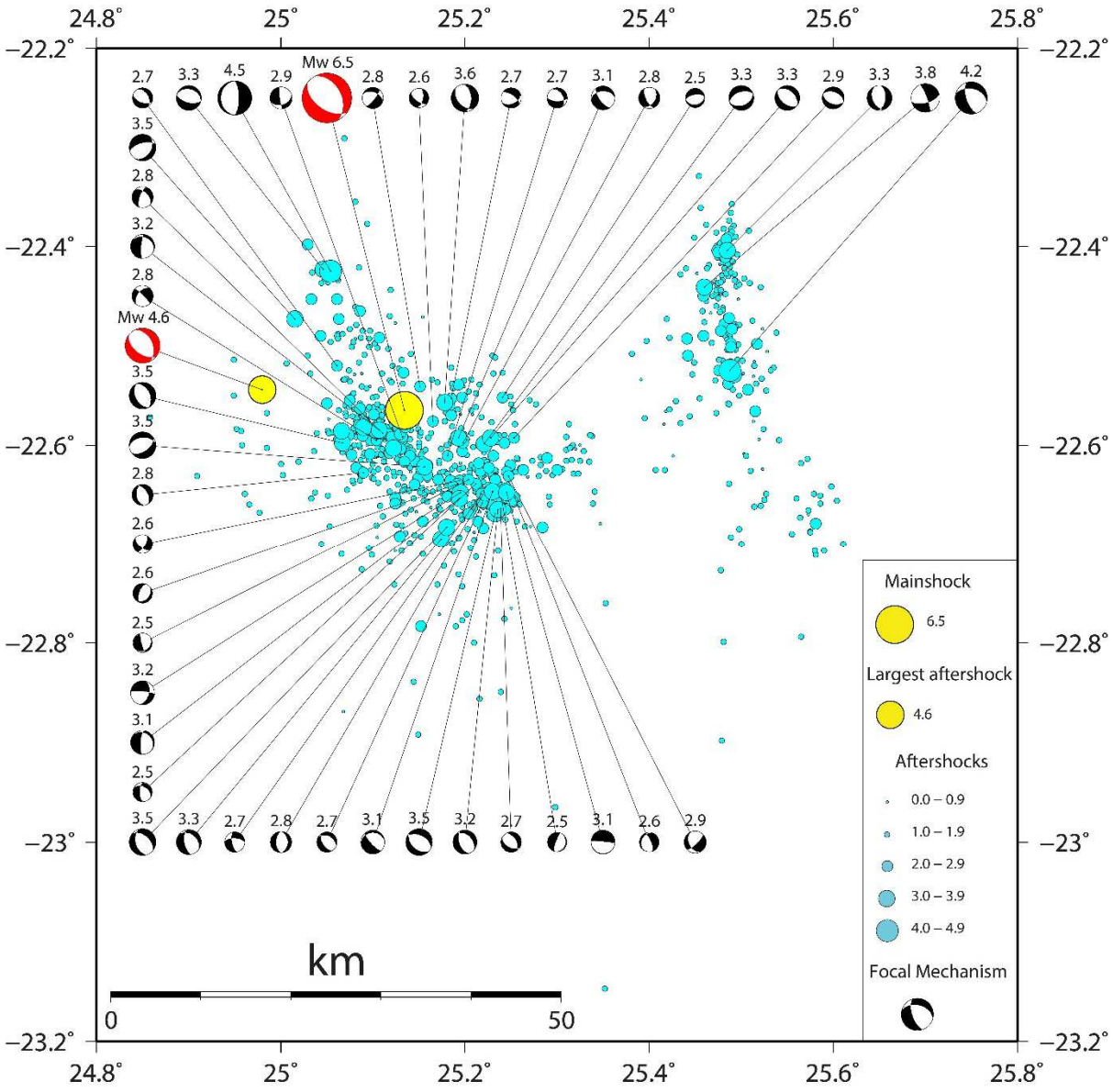

Figure 8. Focal mechanism solutions of 46 selected seismic events (see also Table SM4). Solutions are Schmidt lower hemisphere, the numbers above the solutions give the local magnitude. Aftershock locations are as in Fig. 5(a). Mechanism of mainshock (in red) is from Harvard CMT (https://www.globalcmt.org/CMTsearch.html).

318 Focal mechanisms of aftershocks show normal faulting and few oblique mechanisms
319 (Fig. 8 and Table in SM4). The mainshock and largest aftershock show normal faulting
320 mechanism, with roughly NE and SE dipping nodal planes at 41° and 42°, respectively. The
321 2017 Moiyabana earthquake sequence occurred in an area with no known seismic history,
322 therefore the stress regime is also poorly known. Focal mechanisms of mainshock and 45
323 aftershocks provide the opportunity to obtain information on the kinematic of faulting
324 through stress inversion. For this purpose, two methodologies were used to conduct the stress
325 inversion of the focal mechanisms compiled in this study: the improved right dihedron
326 method (Angelier and Mechler, 1977) and the iterative rotational optimisation method as
327 applied in the WinTensor program (Delvaux 1993; Delvaux and Sperner, 2003).
328 The dihedron method provides an initial approximate stress tensor that is then used as
329 the starting solution for the rotational optimisation method (Delvaux and Barth 2010).
330 Delvaux and Sperner (2003) implemented the rotational optimisation method as an iterative
331 method that can be applied to minimise the misfit between data and model function for each
332 earthquake. During optimisation, only the solutions which are compatible with the lowest
333 misfit are utilised for stress inversion. Out of the 46 focal mechanisms (92 nodal planes) from
334 the database, 30 (60 nodal planes), as well as 14 (28 nodal planes) are compatible with a NE-
335 SW extension under normal faulting regime (Fig. 9). The later analysis with 14 focal
336 mechanisms is performed to test the results after optimising the dataset further for more
337 compatibility.
338 The locations on a normal fault system along NW-SE trending shear zones of the
339 Limpopo Mobile Belt show the influence of the geological background. Most of aftershocks
340 are characterized by average NW (340°) striking with NE dipping fault planes, consistent
341 with the stress distribution and NE-SW extension. The predominant normal faulting
342 mechanism indicates an extensional neotectonic regime in the epicentral area.

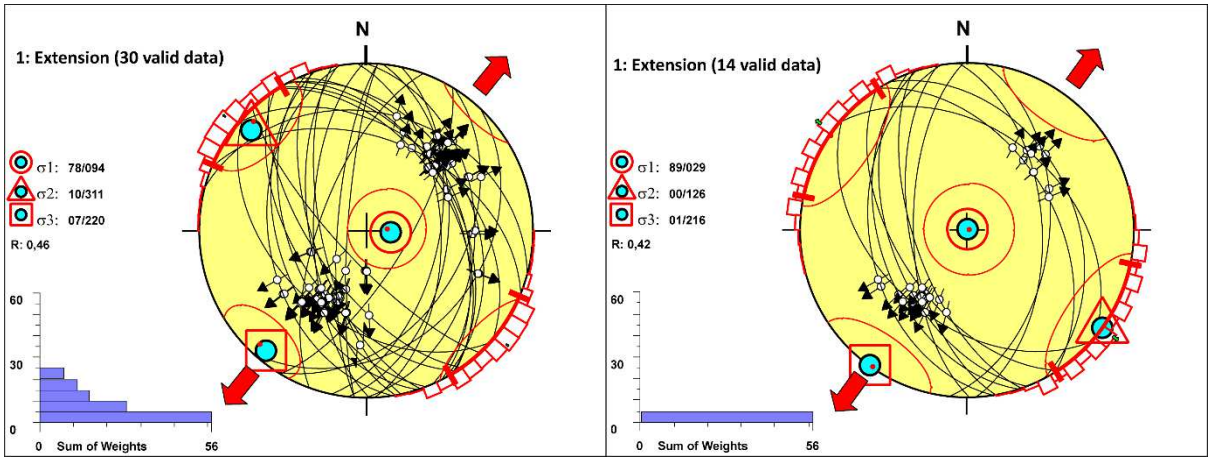

343

344 *Figure 9. Stress inversion of 2017 earthquake aftershocks obtained from the WinTensor*
345 *programme of Delvaux and Sperner (2003). Schmidt diagrams show nodal planes (black*
346 *lines), with Left: Solution from 30 focal mechanisms taking into account all solutions, Right:*
347 *Solution from 14 focal mechanisms with similar strike, dip of fault planes and slip vectors*
348 *(black arrows). The stress tensor distribution (cyan circles) with σ1 in red circle, σ2 in*
349 *triangle, σ3 in square, indicates 220°N and 216°N as the main extension directions (large*
350 *red arrow). The ratio R (0.46 and 0.42) expresses the predominance of extensional stress*
351 *state, and histograms sum of weights that verify the stress tensor.*

352

353 As shown by the analysis of the 2017 Moiyabana earthquake data, its seismotectonic
354 background and nearby geophysical studies such as magnetics and resistivity, the stress field
355 confirms the large-scale extensional forces that may result from elevated heat flow, thermal
356 fluid migration and SW extension of the EARS (Andreoli *et al.*, 1996; Delvaux and Barth,
357 2010; Meghraoui *et al.*, 2016; Materna *et al.*, 2019; Moorkamp *et al.*, 2019; Chisenga *et al.*,
358 2020). The active deformation across the Limpopo Mobile Belt and southern African
359 intraplate domain shows N36E to N40E average extension direction with low level strain rate
360 (~1 nanostrain/yr.; Malservisi *et al.*, 2013), and although the 2017 seismic source is relatively

deep (> 20 km), the existence of thermal fluids and active tectonics with surface deformation suggests the presence of a seismic cycle and associated elastic strain release.

5 Surface deformation

5.1 InSAR Analysis

The SAR (Synthetic Aperture Radar) frames examined in this study are two pairs of ascending Sentinel-1A images that cover the earthquake area (Fig. 10). The used radar images before and after the 2017 mainshock were obtained from the archives of the European Space Agency, and interferograms are processed using GMTSAR (Sandwell *et al*., 2011).

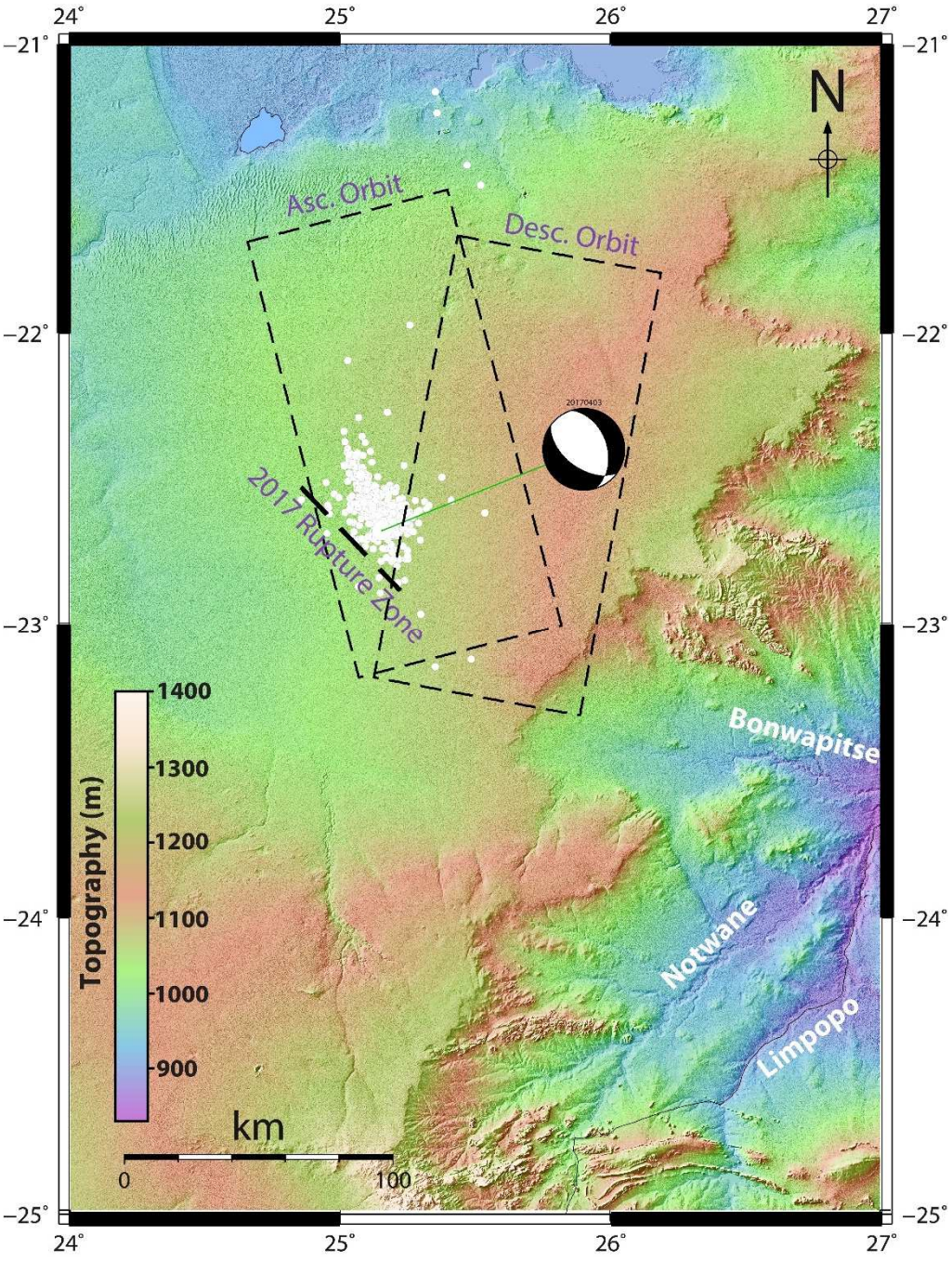

370

371 *Figure 10. Frame of ascending and descending tracks of Sentinel-ESA-SAR images crossing*
372 *the 2017 earthquake area. We observe that only the ascending track covers the whole 2017*
373 *earthquake area. Thick dashed line is the inferred 2017 Moiyabana earthquake rupture zone*
374 *and small white circles show aftershock distribution. Focal mechanism of mainshock is from*
375 *Harvard CMT. Background topography is from SRTM1'.*

376

377 The SRTM Digital Elevation Model (30 m resolution) is used to remove the
378 topographic phase component from the original interferogram (Farr et al., 2007). The spatial
379 filter (Gaussian) is applied to obtain the interferogram (Fig. 11), before proceeding with the
380 unwrapped interferogram using the Snaphu software (Chen and Zebker, 2002). Finally, the
381 unwrapped phase was converted into Line-Of-Sight (LOS) displacement (Fig. 11). The
382 obtained interferogram from a pair of ascending images (2017-03-30 and 2017-04-11;
383 1A/1A) shows clear lobes of LOS displacements (Fig. 11). The interferogram from ascending
384 tracks show a consistent fringe distribution with ~40-km-long and ~20-km-wide NW-SE-
385 trending lobes. The LOS measurements display ground displacement of the SW and NE
386 blocks, respectively, indicating a clear straight limit between lobes that represents the fault
387 zone on the SW edge of the lobe. For ascending tracks, the maximum and minimum values of
388 the LOS displacement range from 4.2 cm to 5.6 cm for interferogram (Fig. 11) from which
389 we estimate a total of 3.86 – 5.15 cm of vertical surface deformation across the fringes. The
390 analysis of the Sentinel-1 interferogram shows a NW-SE elongated and 40-km-long surface
391 deformation consistent with a blind fault rupture geometry. The interferogram also shows a
392 surface deformation with subsidence coincident with the 2017 earthquake sequence location
393 and normal faulting mechanism consistent with the source time function
394 (http://geoscope.ipgp.fr/index.php/en/catalog/).
395

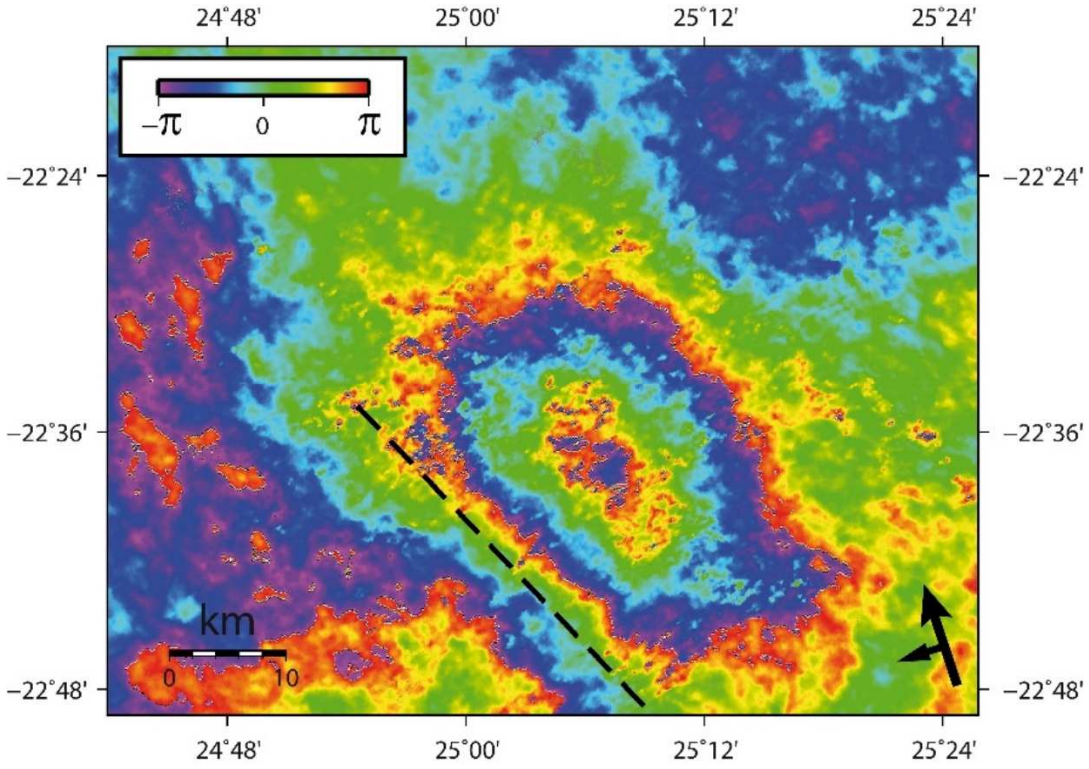

Figure 11. Fringes and lobes of interferogram of the 3rd of April 2017 Botswana earthquake. The dashed line is the projected fault rupture with respect to surface deformation with subsidence (~4.2 – 5.6 cm in LOS). The black arrow (small arrow) is the Sentinel satellite track with side look.

5.2 Earthquake Rupture Model

Rupture and slip models were developed using the ascending phase interferograms and the related coseismic deformation. To minimize the afterslip and/or postseismic effects, the modelling is based on interferograms obtained from the earliest coseismic pairs of Sentinel scenes (Figs 11, 12 a and b). In order to constrain the earthquake rupture geometry and slip distribution at depth, different solutions were tested using fault parameters for the inversion modelling that confirm the InSAR surface deformation.

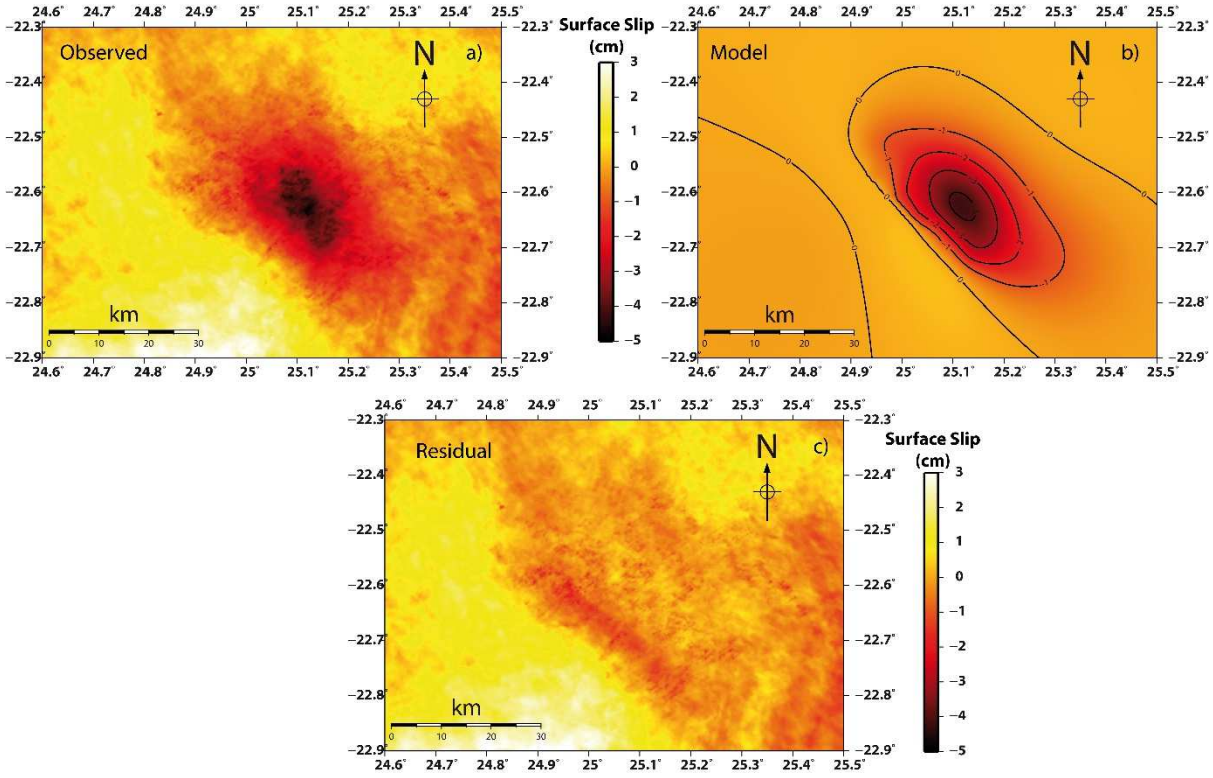

Figure 12 ***a)*** *Unwrapped SAR data interferogram with surface slip distribution.* ***b)*** *Modelling of surface deformation from the inversion of InSAR data.* ***c)*** *Residual of InSAR results versus model.*

The inversion modelling was performed for the dip slip and strike slip component of deformation using the Poly3D method considering triangulated surfaces as discontinuities in a linear, elastic, homogeneous, and isotropic half-space (Maerten *et al.*, 2005; see the details of the method in SM5). The blind coseismic fault coincides at the surface with the inflection area in between the uplift and subsidence lobes (see the fault tip trace in Figs 7b and 11). Considering different fault dimensions and dip angles, we performed a series of inversions that lead to the best fit (with 95% data variance) for the 3D surface slip obtained on the 315°, dipping 45°, -80° rake, ~40-km-long and ~22-km-wide fault geometry with a seismic moment of 3.68 x 10^{18} Nm (Table 1, Fig. 13).

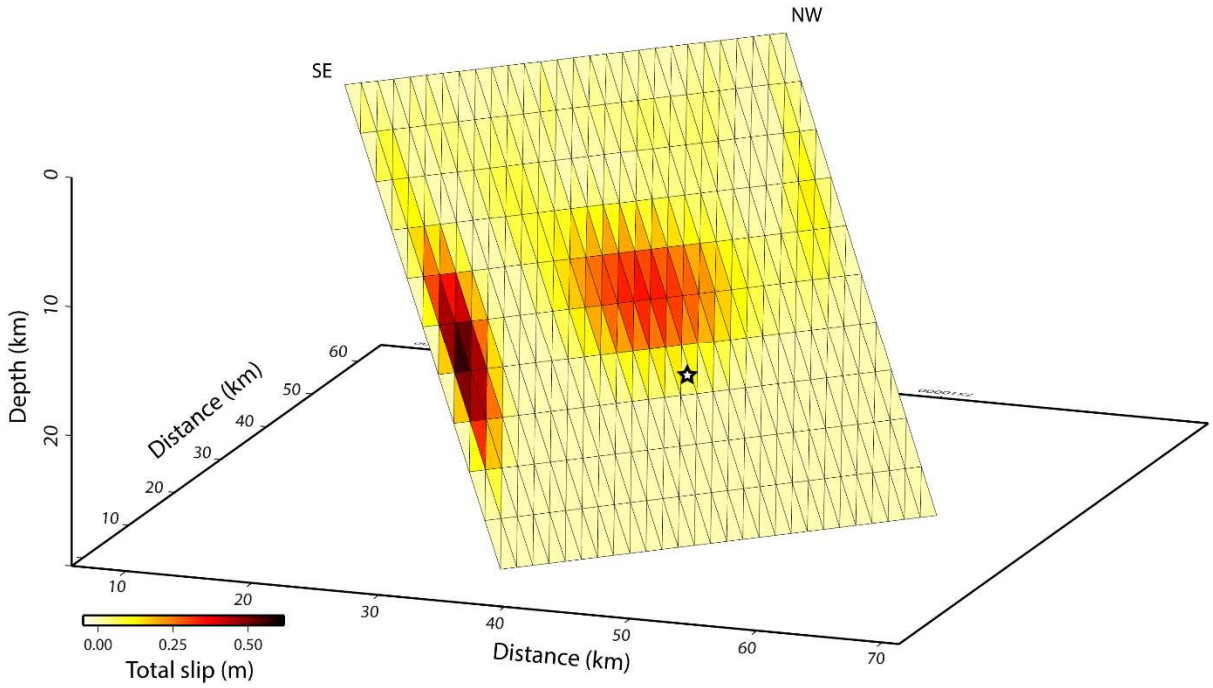

Figure 13. Model of fault rupture with slip distribution reaching 50 cm at depth, as inferred from the inversion of InSAR data and surface deformation. The star indicates the inferred 3rd April 2017 earthquake hypocentre.

The best fitting model shows a maximum slip of 50 cm at a depth of 22 ± 1.5 km and the existence of two asperities along the fault which agrees with the observed western seismic cluster (Figs 7a and b). Observed interferograms are compared to the inversion models in order to minimize the residual fringes with RMS misfit (Fig. 12c). The residual signals in Figure 12c (~1 cm) could be attributed to the atmospheric delay signal, the unwrapping error, and the surface motion caused by the post-seismic afterslip and aftershocks. As shown in Figure 14, the modelling allows to test the 0.744 cm RMS against the 0.4 smoothing and 0.23 roughness of the coseismic rupture. The location of the InSAR displacement and inferred blind fault rupture with NW-SE elongated lobes suggests a correlation with ~30-km-long

buried fault that belongs to the Limpopo Mobile Tectonic Belt and can be correlated to the Khurutse fault scarp visible further southeast.

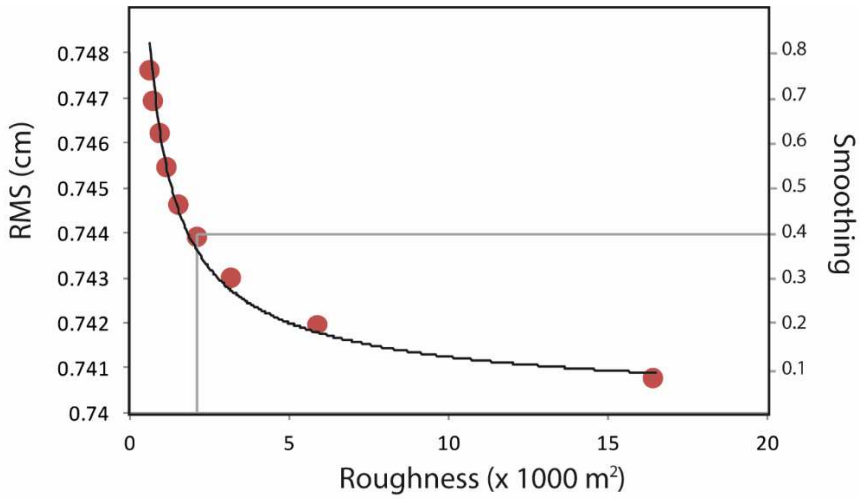

Figure 14. RMS misfit (minimize the residuals) obtained from the comparison between interferograms and inversion models of Figures 12a and b), residual of Figure 12c, and slip distribution of Figure 13. The 0.744 cm RMS and 0.4 smoothing (grey lines) correspond to the best compromise for the slip distribution on the fault plane.

6 Khurutse Fault Scarp and Long-term Seismic Cycle

The interplay between tectonic processes which build up topography and the surface processes which tear them down over time, in days to millions of years, are what defines tectonic geomorphology (Burbank and Anderson, 2001). Thus, the study of tectonic geomorphology can indicate geological linear structures from past fault activities. Such studies can be done using for instance GPS data, providing a rate of deformation on the Earth's surface such as the spatial deformation pattern caused by an earthquake. The displacement field of the earthquake can be measured from the deformed ground surface,

subsequently delineating the relationship between seismic characteristics, displacement gradient and rock properties.

The Khurutse fault scarp is visible on topographic maps (both SRTM 90 m and 30 m resolution; Farr *et al.*, 2007) southeast of the 2017 M_W 6.5 earthquake (Figs 15, 16 and 17a). Four cross section profiles of the faults scarp (Fig. 17b) were plotted using the differential GPS data collected at sites indicated in (Fig. 17a).

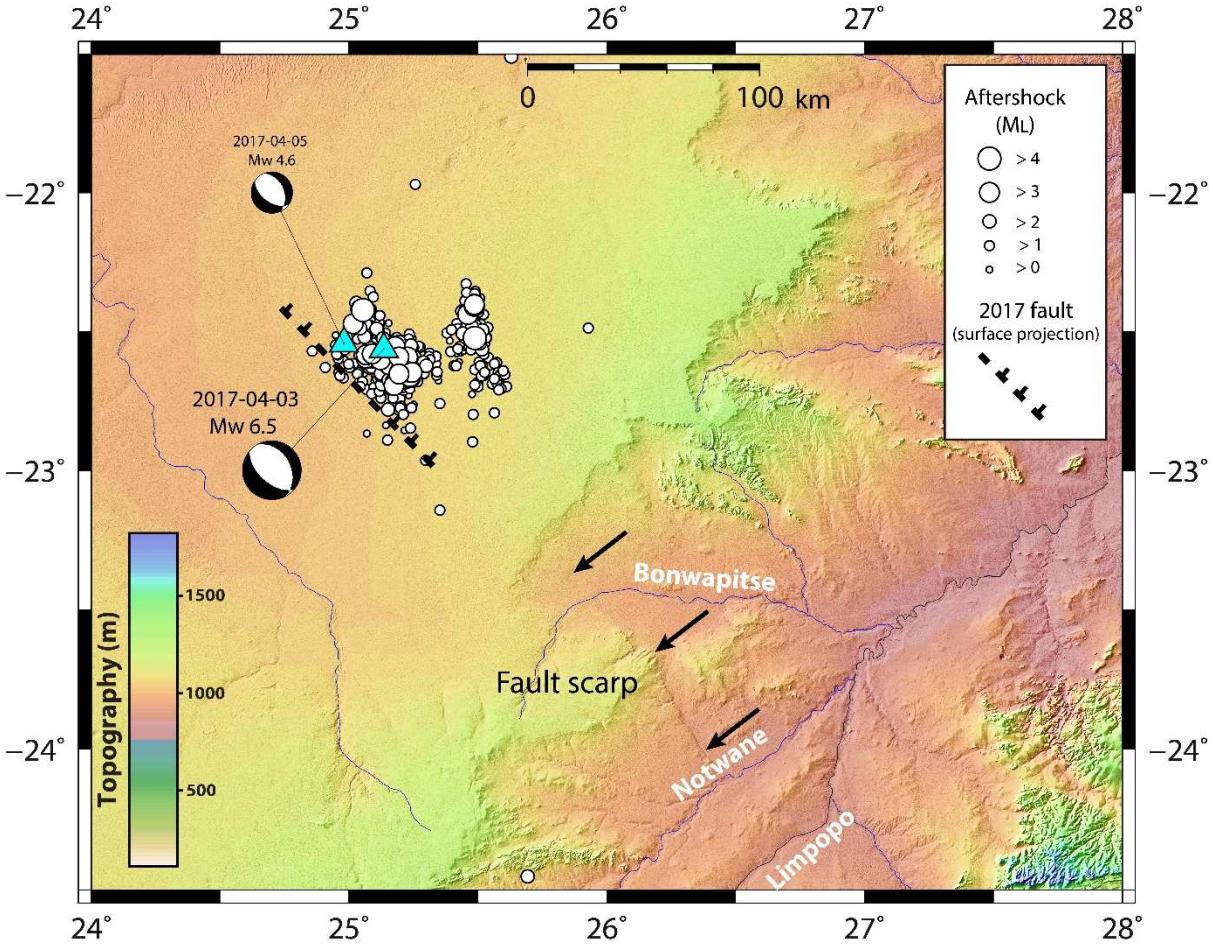

Figure 15: Identification of the Khurutse cumulative fault scarp (black arrows) southeast of the 2017 earthquake rupture indicated using a dashed line located from the projection of InSAR rupture (see Fig. 11). Also shown are the focal mechanisms of the mainshock and largest aftershock as presented in Tables 1 and SM4. Details of Khurutse fault scarp

morphology are in landscape photos of Fig. 16 and map of Fig 17a. Background topography is from Shuttle Radar Topography Mission (SRTM) 1" data.

Figure 16. Khurutse fault scarp with significant topographic offset. Left is fault scarp (view facing east) near profile A (24.004°S, 26.376°E) of Figs 17a and b; Right is fault scarp (view facing west) near profile B (23.967S, 26.350E) of Figs 17a and b. Fault scarps show composite and cumulative geomorphic structures that suggest repeated coseismic surface deformation.

The exposed NNW-SSE trending and ~80-km-long Khurutse fault scarp southeast of the 2017 epicentral area is aligned with the 2017 coseismic rupture and aftershock sequence (Fig 15). The escarpment is orthogonal to two main erosion valleys formed by different rivers and streams and crosses mainly Phanerozoic sediments. To the southeast, and although crossing an erosional valley, the fault scarp morphology is prominent and visible on left and right river channel banks (Fig. 17a) (Williamson, 1996). Differential GPS measurements of profiles across the fault scarp shows topographic offset ranging between 16.6 ± 1 m and 43.5 ± 1 m (Fig. 17b). All geomorphic profiles display a composite and sharp scarp morphology that reflects a cumulative surface deformation. The fault scarp height variation depends on the background geology and erosion effect and shows minimum and maximum topographic

offsets in profiles A and D, respectively. That the linear morphology and scarp shape remain visible in the Limpopo Mobile Belt, is indicative of recent tectonic movement that may have resulted from incremental surface slip during past earthquakes.

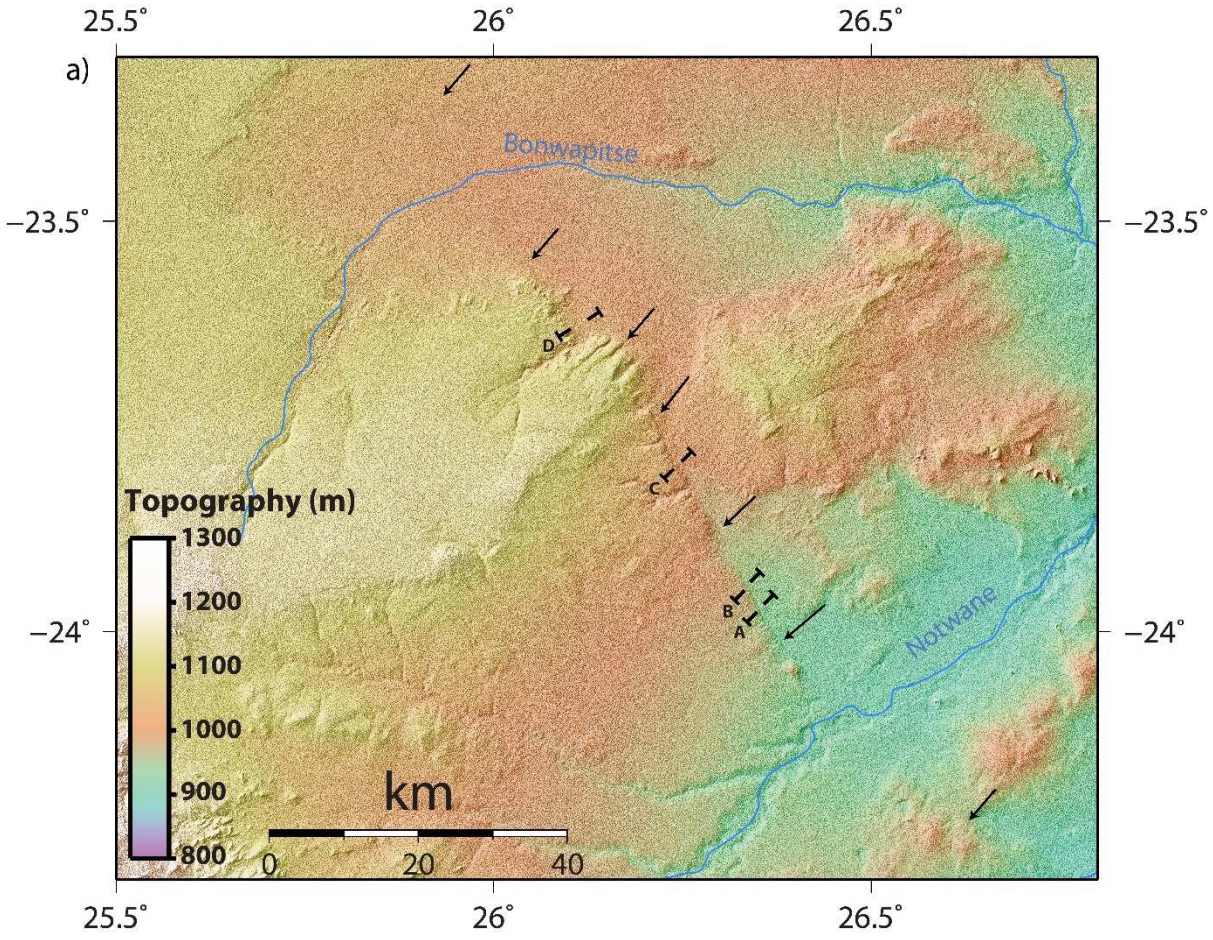

Figure 17. ***a)*** *Detail of the Khurutse fault scarps (arrows, see also arrows in Fig. 15) with location of the cross-section profiles of Fig. 17(b) denoted A to D (background topography from SRTM 1" data).*

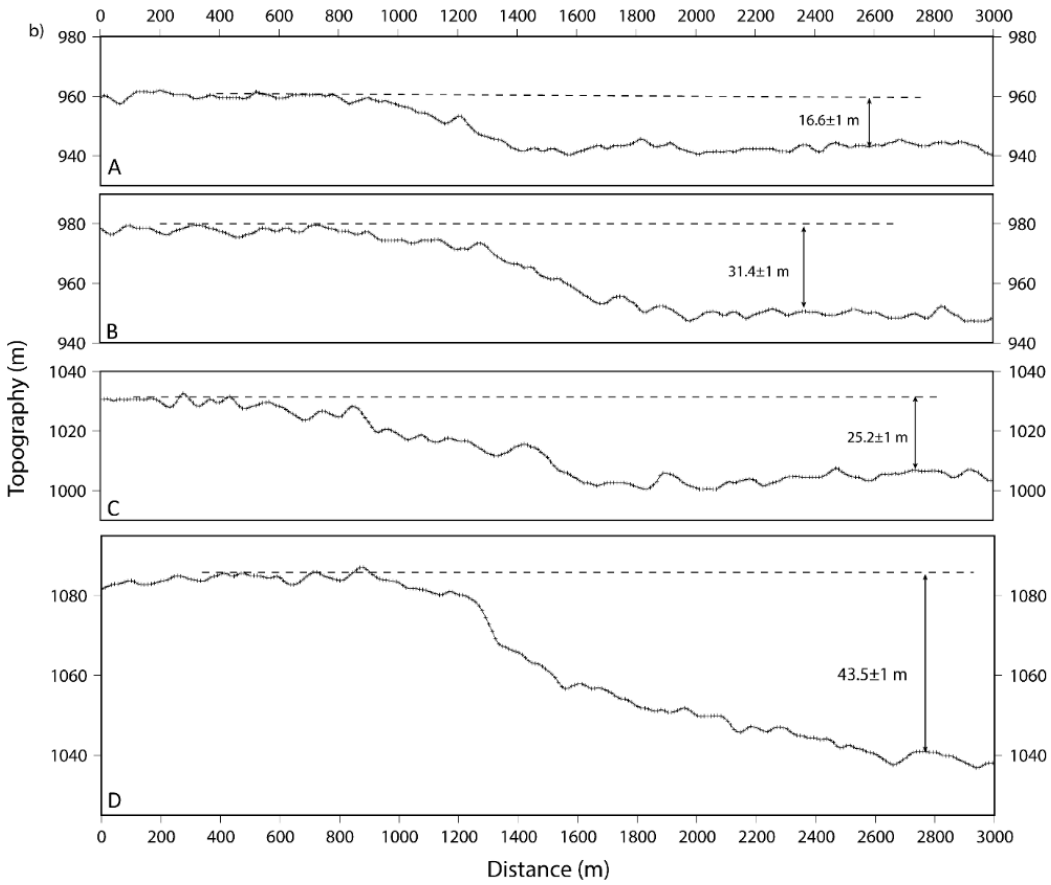

Figure 17. ***b)*** *Khurutse fault scarp cross-sections with measured geomorphic offsets, in meters.*

7 Discussion

Although previous studies using teleseismic data and InSAR provided initial results on the 2017 Moiyabana earthquake, our investigations present the integration of near field and remote sensing studies including seismology, seismotectonic and Radar satellite images. Field investigations using six portable seismic stations supplemented with data from nearby permanent broadband seismic stations and tectonic geomorphology combined with the study of InSAR data, brought new insights in the study of the 2017 Moiyabana earthquake (M_W 6.5). Focal mechanism solutions indicate that the mainshock ruptured on a NW-SE trending blind normal fault. More than 900 aftershocks shed light on the fault rupture geometry within ~30 km depth of the Limpopo Mobile Belt in Botswana. Two aftershock sequences range

between 5 and 30 km depth and show the complexity of the active crustal structure that delineates a NW-SE trending, and 20 to 30 km wide graben structure. Most of the aftershocks are of normal faulting mechanism with a general NE-SW extension direction confirmed by the stress tensor inversion.

Interferograms obtained from the analysis of Sentinel 1A images display 2 to 3 fringes (from which we infer 3.86 to 5.15 cm vertical displacement) that form two lobes coincident with the mainshock and aftershock locations. The modelling of coseismic rupture and slip distribution obtained from the inversion of surface deformation suggests ~40-km-long and ~22-km-wide fault geometry with the fault striking 315°, dipping 45°, with -80° rake, with two asperities and a maximum 50 cm slip distribution. This is different from Albano *et al.* (2017) InSAR inferred coseismic model of 20- km-long rupture plane, dipping 65° to the northeast, with a right-lateral component, and 2.7 m maximum slip at depth. In the absence of near field seismicity data and using InSAR results with a Bayesian estimate of source parameters, Gardonio *et al*. (2018) suggest both ~17° and ~73° dipping fault planes and a poorly estimated hypocentre depth of 29 ± 4 km. From the inversion of InSAR results coupled with geophysical (aeromagnetic and gravity) data, Kolawole *et al.* (2017) test several fault patches and estimate 21 to 24 km hypocentre depth on a 53° NE dipping fault plane, comparable with our 22 ± 1.5 km depth and 45° NE dipping fault plane.

7.1 Rifting propagation within intraplate southern Africa

Large intraplate earthquakes ($M_W \geq 6$) in southern Africa may result from complex continental tectonics and elastic strain release with continuum deformation rather than movements of rigid blocks (Scholz *et al.*, 1976; Reeves *et al.*, 2004). The rifting of the Ghanzi-Chobe Proterozoic Belt, due to the extensional forces during the Kibaran Orogeny, gave rise to the beginning of the Okavango rifting (Leseane *et al.*, 2015). This is the area

where a significant seismic sequence occurred on 11 September 1952 with M_L 6.1 and another of M_L 6.7 on 11 October 1952. The Zoetfontein fault is another active zone in Botswana which has been known to be seismically active, thus revealing a background seismicity associated with long-term deformation and faulting (Dorland *et al.,* 2006). Its boundary with the Zimbabwe Craton is on the Limpopo-Shashe Thrust Zone (Ranganai *et al.*, 2002). The 2017 Moiyabana earthquake reveals the existence of a NW-SE trending active normal fault zone within the Limpopo Mobile Belt in Botswana. Daly *et al.* (2020) investigated the Okavango normal fault system using SRTM1" and Pleaides images and identified NE to ENE trending faults with evidence of vertical displacement. At a larger scale, normal faulting mechanisms of Moiyabana, Okavango and Machaze active zones reflect the complex crustal deformation within the Nubian Plate (Kinabo *et al.*, 2008; Fenton and Bommer 2006; Fonseca *et al.*, 2014). As compared to the region where the 2017 Moiyabana earthquake is located, the EARS is much more seismically active, since it is a divergent plate boundary. Furthermore, the 2017 Moiyabana earthquake and Okavango active zones with related seismotectonic framework appear as an extension of the EARS to the west (Kinabo *et al.*, 2008). Hence, the Limpopo Mobile Belt and Okavango active zones mark the possible development of new rifting zones within Nubia active plate interior.

7.2 Seismotectonics of intraplate earthquakes in southern Africa

A detailed analysis of the mainshock and aftershocks of the 2017 Moiyabana earthquake sequence in Botswana and related surface deformation lead to a better understanding of the intraplate seismic activity in southern Africa. The coseismic fault has been documented by means of the two seismic sequences that illustrate the rupture geometry at depth. The use of two different software packages (SEISAN and HypoDD) for the earthquake locations provides an insight to the seismic sequence at depth that illustrates the fault rupture geometry.

552 The coincidence in the location of mainshock, aftershocks, InSAR lobe results, and
553 composite fault scarp reflects the long-term active deformation in the intraplate tectonic
554 environment. Although the strain rate is rather low (~1 nanostrain/yr.), the occurrence of the
555 2017 Moiyabana earthquake constrains us to classify the Limpopo Mobile Belt as an active
556 tectonic zone with a recurrent seismic strain release. These observations do not support the
557 suggested hypothesis that the 2017 Moiyabana earthquake can be due to transient
558 perturbations of local stresses due to pore fluid pressure (Gardonio *et al.*, 2018). The
559 recurrence interval of large seismic events with surface deformation may reach several
560 thousands of years that results from long-term but persistent seismic cycles (Camelbeeck and
561 Meghraoui, 1998). In some regions such as Mongolia, major earthquakes in 1905 and 1957
562 with M_W 8 and 8.5, respectively, leave evidence of multiple rupture over the years (Chéry *et*
563 *al.*, 2001). The study of recent earthquakes with near field investigations is crucial for a better
564 understanding of the intraplate seismicity and active deformation in intraplate southern
565 Africa.
566

567 # 8 Conclusion

568 The near field study of the 2017 Moiyabana earthquake (Mw 6.5) provides data and
569 results on the crustal deformation of the intraplate tectonic domain of southern Africa. The
570 detailed mainshock and aftershocks analysis shows a seismic sequence that suggests a fault-
571 rupture geometry in agreement with normal focal mechanisms. The aftershocks analysis and
572 focal mechanism solutions show predominately normal faulting that agrees with the NE-SW
573 extensional stress regime in the region. Two distinct NW-SE to N-S trending aftershock
574 sequences of more than 900 earthquakes processed using SEISAN, of which 699 aftershocks
575 were relocated using the HypoDD program, are concentrated between 10 and 30 km depth.
576 The distance between the two sequences being ~20 km, seismic events depict a graben-like

577 structure where the mainshock and largest aftershock are located within the western
578 sequence. The InSAR analysis shows the colocation of surface deformation with the western
579 earthquake sequence and allows the modelling of a NW-SE trending fault rupture, dipping
580 NE with an average 50 cm slip distribution and a seismic moment M_o 3.68 x 10^{18} Nm (Mw
581 6.4). SE of the epicentral area, we identified the NNW-SSE to NW-SE trending composite
582 and sharp scarp morphology of the Khurutse fault scarp that aligns with the 2017 Moiyabana
583 earthquake rupture. The active Okavango and Zoetfontein fault region, in the north and south
584 of the Moiyabana earthquake location, respectively; indicate that the southern African
585 continental region is active. In addition, the Khurutse fault scarp reflects a cumulative surface
586 deformation, clearly highlighting the presence of a seismic cycle in this intraplate context.

Acknowledgements:

The work is supported by the Council of Geoscience (Pretoria), the Institut de la Terre et Environnement de Strasbourg (ITES) and UNESCO IGCP-659 project, and TM benefited from a Campus France scholarship of the French Embassy in Pretoria. The Council of Geoscience and Botswana Geoscience Institute provided field assistance for seismic stations deployment and for DGPS measurements of the Khurutse fault scarp. We are thankful to the European Space Agency for providing the Sentinel SAR images. We are indebted to Sophie Lambotte (ITE Strasbourg) for assistance in the relocation processing, Mohamed Khelif (CRAAG, Algiers) for assistance with SEISAN, Damien Delvaux for assistance with WinTensor program and Klaus Hinzen (University of Cologne) for discussion on an earlier version of manuscript. All figures have been produced using Generic Mapping Tools (Wessel & Smith 1998). We are also thankful to the Editor Mohamed G Abdelsalam and reviewer Sarah Stamps for their comments that improve the presentation of our manuscript.

References

Albano, M., Polcari, M., Bignami, C., Moro, M., Saroli, M., Stramondo, S., 2017. Did Anthropogenic Activities Trigger the 3 April 2017 Mw 6.5 Botswana Earthquake?, Remote Sens., 9 (10), 1028 – 1040.

Andreoli, M. A. G., Doucoure, M., Van Bever Donker, J., Brandt, D., Andersen, N. J. B., 1996. Neotectonics of southern Africa: A review, Afr. Geosci. Rev., 3(1), 1–16.

Angelier, J. Mechler, P., 1977. Sur une méthode graphique de recherche des contraintes principales également utilisable en tectonique et en séismologie: la méthode des dièdres droits, Bull. Soc. géol. Fr., 19, 1309 – 1318.

611 Begg, G. C., Griffin, W. L., Natapov, L. M., O'Reilly, S. Y., Grand, S. P., O'Neill, C. J.,
612 Hronsky, J. M. A., Poudjom Djomani, Y., Swain, C.J., Deen, T., Bowden, P., 2009.
613 The Lithospheric Architecture of Africa: Seismic Tomography, Mantle Petrology, and
614 Tectonic Evolution, Geosphere, 5, 23 – 50.
615 Bent, A. L., 1994. The 1989 (Ms 6.3) Ungava, Quebec, earthquake: A complex intraplate
616 event, Bull. Seismol. Soc. Am., 84(4), 1075 – 1088.
617 Brown, R., Gernon, T., Stiefenhofer, J., Field, M., 2008. Geological constraints on the
618 eruption of the Jwaneng Centre kimberlite pipe, Botswana. J. Volcanol. Geotherm.
619 Res., 174 (1), 195 – 208.
620 Burbank, D. W., Anderson, R. S., 2001. Tectonic geomorphology, Blackwell Science Ltd,
621 Oxford, United Kingdom.
622 Calais, E., T. Camelbeeck, Stein, S., Liu, M., Craig, T. J., 2016. A new paradigm for large
623 earthquakes in stable continental plate interiors, Geophys. Res. Lett, 43(20), 10621 –
624 10637.
625 Camelbeeck, T., Meghraoui, M., 1998. Geological and geophysical evidence for large
626 paleoearthquakes with surface faulting in the Roer Graben (northwest Europe),
627 Geophys. J. Int., 132, 347 – 362.
628 Chéry, J., Carretier, S., Ritz, J.-F., 2001. Postseismic stress transfer explains time clustering
629 of large earthquakes in Mongolia, Earth Planet. Sci. Lett., 194(1–2), 277–286,
630 doi:10.1016/S0012-821X(01)00552-0.
631 Chisenga, C., Van der Meijde, M., Yan, J., Fadel, I., Atekwana, E. A., Steffen, R.,
632 Ramotoroko, C., 2020. Gravity derived crustal thickness model of Botswana: Its
633 implication for the Mw 6.5 April 3, 2017, Botswana earthquake, Tectonophysics, 787.
634 https://doi.org/10.1016/j.tecto.2020.228479

635 Clark, D., Dentith, M., Wyrwoll, K. H., Yanchoul, L., Dent, V., Featherstone, C., 2008. The
636 Hyden fault scarp, Western Australia: paleoseismic evidence for repeated Quaternary
637 displacement in an intracratonic setting, Aust. J. Earth Sci., 55, 379 – 395.
638 Crone, A. J., Machette, M. N., Bowman, J. R., 1997. Episodic nature of earthquake activity in
639 stable continental regions revealed by palaeoseismicity studies of Australian and North
640 American quaternary faults, Aust. J. Earth Sci., 44(2), 203–214.
641 Daly, M. C., Green, P., Watts, A. B., Davies, O., Chibesakunda, F., Walker, R., 2020.
642 Tectonics and landscape of the Central African Plateau and their implications for a
643 propagating Southwestern Rift in Africa, Geochemistry, Geophys. Geosystems, 21, 1 –
644 37, doi.org/10.1029/2019GC008746.
645 Delvaux, D., 1993. The TENSOR program for paleostress reconstruction: examples from the
646 east African and the Baikal rift zones. EUG VII Strasbourg, France, 4–8 April 1993.
647 Abstract supplement N°1 to Terra Nov. 5: 216.
648 Delvaux, D. B., Sperner, 2003. New aspects of tectonic stress inversion with reference to the
649 TENSOR program. In: New Insights into Structural Interpretation and Modelling (D.
650 Nieuwland Ed.). Geological Society, London, Special Publications 212: 75 – 100.
651 Delvaux, D., Barth, A., 2010. African stress pattern from formal inversion of focal
652 mechanism data. Implications for rifting dynamics, Tectonophysics, 482, 105 – 128.
653 Dorland, H. C., Beukes, N. J., Gutzmer, J., Evans, D. A. D., Armstrong, R. A., 2006. Precise
654 SHRIMP U-Pb zircon age constraints on the lower Waterberg and Soutpansberg
655 Groups, South Africa, S Afr J Geol, 109, 139 – 156.
656 Fadel, I., Paulssen, H., van der Meijde, M., Kwadiba, M., Ntibinyane, O., Nyblade, A.,
657 Durrheim, R., 2020. Crustal and Upper Mantle Shear Wave Velocity Structure of
658 Botswana: The 3 April 2017 Central Botswana Earthquake Linked to the East African
659 Rift System, Geophys. Res. Lett, 47(4).

660 Farr, T. G., Rosen, P. A., Caro, E., Crippen, R., Duren, R., Hensley, S., Kobrick, M., Paller,
661 M., Rodriguez, E., Roth, L., Seal, D., Shaffer, S., Shimada, J., Umland, J., Werner,
662 M., Oskin, M., Burbank, D., Alsdorf, D., 2007. The Shuttle Radar Topography
663 Mission, Rev. Geophys., 45, RG2004, doi:10.1029/2005RG000183.
664 Fairhead, J., Henderson, N., 1977. The seismicity of Southern Africa and incipient rifting,
665 Tectonophysics, 41, 19–26.
666 Fenton, C., Bommer, J., 2006. The Mw 7 Machaze, Mozambique, earthquake of 23 February
667 2006, Seism. Res. Lett., 77, 426–439, doi:10.1785/gssrl.77.4.426.
668 Fonseca, J.F.B.D., Chamussa, J., Domingues, A., Helffrich, G., Antunes, E., van Aswegen,
669 G., Pinto, L.V., Cust_odio, S., Manhiça, V.J., 2014. MOZART: a seismological
670 investigation of the east African rift in Central Mozambique. Seismol Res. Lett. 85 (1),
671 108 – 116.
672 Fourie, C. J. S., Henry, G., Maré, L. P., 2014. The structure of the Karoo-age Ellisras Basin in
673 Limpopo Province, South Africa in the light of new airborne geophysical data: a
674 preliminary report, S Afr J Geol, 117 (2), 207 – 224.
675 Gardonio, B., Jolivet, R., Calais, E., Leclère, H., 2018. The April 2017 Mw6.5 Botswana
676 Earthquake: An Intraplate Event Triggered by Deep Fluids, Geophys. Res. Lett, 45
677 (17), 8886 – 8896.
678 Hartnady, C., 1990. Seismicity and plate boundary evolution in Southeastern Africa, S. Afr.
679 J. Geol., 93, 473–484.
680 Hough, S. E., Page, M., 2011. Toward a consistent model for strain accrual and release for
681 the New Madrid Seismic Zone, central United States, J. Geophys. Res., 116, B03311,
682 doi:10.1029/2010JB007783.
683 Johnston, A.C., 1996a. Seismic moment assessment of earthquakes in stable continental
684 regions—I. Instrumental seismicity, Geophys. J. Int., 124 (2), 381– 414.

685 Johnston, A.C., 1996b. Seismic moment assessment of earthquakes in stable continental
686 regions—II. Historical seismicity, Geophys. J. Int., 125 (3), 639 – 678.
687 Kinabo, B., Hogan, J., Atekwana, E., Abdel Salam, M. Modisi, M., 2008. Fault growth and
688 propagation during incipient continental rifting: inside from a combined aeromagnetic
689 and Shuttle Radar Topography Mission digital elevation model investigation of the
690 Okavango Rift Zone, northwest Botswana, Tectonics, 27, doi:10.1029/2007TC002154.
691 Kolawole, F., Atekwana, E. A., Malloy, S., Stamps, D. S., Grandin, R., Abdelsalam, M. G.,
692 Leseane, K., Shemang E. M., 2017. Aeromagnetic, gravity, and Differential
693 Interferometric Synthetic Aperture Radar (DInSAR) analyses reveal the causative fault
694 of the 3 April 2017 Mw 6.5 Moiyabana, Botswana Earthquake, Geophys. Res. Lett, 44,
695 8837 – 8846.
696 Lekula, M., Lubczynskia, M. W., Shemang, E. M., 2018. Hydrogeological conceptual model
697 of large and complex sedimentary aquifer systems – Central Kalahari Basin, Phys
698 Chem Earth, 106, 47 – 62.
699 Leseane, K., Atekwana, E. A., Mickus, K. L., Abdelsalam, M. G., Shemang E. M.,
700 Atekwana, E. A., 2015. Thermal perturbations beneath the incipient Okavango Rift
701 Zone, northwest Botswana, J. Geophys. Res. Solid Earth, 120 (2), 1210 – 1228.
702 Lienert, B. R., Berg, E., Frazer, L. N., 1986. Hypocenter: an earthquake location method
703 using centered, scaled, and adaptively damped least squares, Bull. Seismol. Soc. Am.,
704 76(3), 771 – 783.
705 Lienert, B. R., Havskov, J., 1995. A Computer Program for Locating Earthquakes Both
706 Locally and Globally, Seismol. Res. Lett., 66 (5), 26 – 36.
707 Malservisi, R., Hugentobler, U., Wonnacott, R., Hackl, M., 2013. How rigid is a rigid plate?
708 Geodetic constraint from the TrigNet CGPS network, South Africa, Geophys. J. Int.,
709 192, 918 – 928.

710 Manzunzu, B., Midzi, V., Mangongolo, A., Essrich, F., 2017. The aftershock sequence of the
711 5 August 2014 Orkney earthquake (ML 5.5), South Africa, J. Seismol., 21, 1323 –
712 1334.
713 Maerten, F., Resor, P., Pollard, D., Maerten, L., 2005. Inverting for slip on three-dimensional
714 fault surfaces using angular dislocations, Bull. Seismol. Soc. Am., 95 (5), 1654 – 1665.
715 Materna, K., Wei, S., Wang, X., Heng, L., Wang, T., Chen, W., Salman, R., Bürgmann, R.,
716 2019. Source characteristics of the 2017 Mw6.4 Moijabana, Botswana earthquake, a
717 rare lower-crustal event within an ancient zone of weakness, Earth Planet Sci Lett, 506,
718 348 – 359.
719 Meghraoui, M., Amponsah, P., Ayadi, A., Ayele, A., Ateba, B., Bensuleman, A., Delvaux,
720 D., El Gabry, M., Fernandes, R., 2016. The Seismotectonic Map of Africa, Episodes,
721 39 (1), 9 – 18.
722 Midzi, V., Saunders, I., Brandt, M. B. C., Molea, T., 2010. 1-D velocity model for use by the
723 SANSN in earthquake location, Seismol. Res. Lett., 81 (3), 460 – 466.
724 Midzi, V., Saunders, I., Manzunzu, B., Kwadiba, M. T., Jele, V., Mantsha, R., Marimira, K.
725 T., Mulabisana, T. F., Ntibinyane, O., Pule, T., Rathod, G. W., Sitali, M., Tabane, L.,
726 van Aswegen, G., Zulu, B. S., 2018. The 03 April 2017 Botswana M6.5 earthquake:
727 Preliminary results, J. African Earth Sci., 143, 187 – 194.
728 Modisi, M., Atekwana, E., Kampunzu, A., Ngwisanyi, 2000. Rift kinematics during the
729 incipient stages of continental extension: evidence from the nascent Okavango Rift
730 basin, northwest Botswana, Geology, 28, 939–942.
731 Moorkamp, M., Fishwick, S., Walker, R. J., Jones, A. G., 2019. Geophysical evidence for
732 crustal and mantle weak zones controlling intra-plate seismicity – the 2017 Botswana
733 earthquake sequence, Earth Planet Sci Lett, 506, 175 – 183.

734 Nguuri, T. K., Goree, J., James, D. E., Webb, S. J., Wright, C., Zengen, T. G., Gwavava, O.,
735 Snoke, J., A Kaapvaal Seismic Group, 2001. Crustal structure beneath southern Africa
736 and its implications for the formation and evolution of the Kaapvaal and Zimbabwe
737 cratons, Geophys. Res. Letters 28, 13, 2501-2504.
738 Njoroge, M., R. Malservisi, Voytenko, D., Hackl, M., 2015. Is Nubia Plate Rigid? A geodetic
739 study of the relative motion of different cratonic areas within Africa, International
740 Association of Geodesy Symposia, p 1-9, doi:10.1007/1345_2015_212
741 Okada, Y., 1985. Surface deformation due to shear and tensile faults in a half-space, Bull.
742 Seismol. Soc. Am., 75 (4), 1135 – 1154.
743 Olebetse, T.A., Mmese, M.L., Simon, R.E., Maritinkole, J., 2020. Some Foreshocks and
744 Aftershocks Associated with the Moiyabana Earthquake of 2017 in Botswana. Int. J.
745 Geosci., 11, 238-250. https://doi.org/10.4236/ijg.2020.114013
746 Ottemöller, L., Voss, P., Havskov, J., 2018. SEISAN Earthquake Analysis Software for
747 Windows, Solaris, Linux and Macosx. Bergen.
748 Rajendran, C. P., Rajendran, K., John, B., 1996. The 1993 Killari (Latur), central India,
749 earthquake: An example of fault reactivation in the Precambrian crust, Geology 24,
750 651–654.
751 Ranganai, R. T., Kampunzu, A. B., Atekwana, E. A., Paya, B. K., King, J. G., Koosimile, D.
752 I., Stettler, E. H., 2002. Gravity evidence for a larger Limpopo Belt in southern Africa
753 and geodynamic implications, Geophys J Int., 149 (3), F9 – F14.
754 Reeves, C., de Wit, M. Sahu, B., 2004. Tight reassembly of Gondwana exposes phanerozoic
755 shears in Africa as global tectonic players, Gondwana Res., 7, 7–19.
756 Roering, C., van Reenen, D. D., Smit, C. A., Barton, J. M., de Beer, J. H., de Wit, M. J.,
757 Stettler, E. H., van Schalkwyk, J. F., Stevens, G., Pretorius, S., 1992. Tectonic model
758 for the evolution of the Limpopo Belt, Precambrian Res., 55, 539 – 552.

759 Ross, Z. E., Meier, M., Hauksson, E., 2018. P wave arrival picking and first-motion polarity
760 determination with deep learning, J. Geophys. Res. Solid Earth, 123 (6), 5120 – 5129.
761 Sandwell, D., Mellors, R., Tong, X., Wei, M., Wessel, P., 2011. GMTSAR: An InSAR
762 Processing System Based on Generic Mapping Tools. UC San Diego: Scripps
763 Institution of Oceanography. Retrieved from:
764 http://escholarship.org/uc/item/8zq2c02m.
765 Saria, E., Calais, E., Stamps, D.S., Delvaux, S. Hartnady, C.J.H., 2014. Present-day
766 kinematics of the East African Rift, J. geophys. Res., 119, doi:10.1002/2013JB010901.
767 Saunders, I., Brandt, M.B.C., Molea, T.T., Akromah, L. Sutherland, B., 2010. Seismicity of
768 Southern Africa during 2006 with special reference to the Mw 7 Machaze earthquake. S
769 Afr J Geol, 113, 4, 369-380.
770 Scholz, C., Kocynski, T. Hutchins, D., 1976. Evidence for incipient rifting in Southern
771 Africa, Geophys. J. R. astr. Soc., 44, 135–144.
772 Stamps, D. S., Flesch, L. M., Calais, E., Ghosh, A., 2014. Current kinematics and dynamics
773 of Africa and the East African Rift System, J. Geophys. Res. Solid Earth, 119, 5161 – 5186,
774 doi:10.1002/2013JB010717.
775 Stamps, D. S., Saria, E., Kreemer, C., 2018. A Geodetic Strain Rate Model for the East
776 African Rift System, Sci. Rep., 8(1), 1 – 8.
777 Thomas, A., 2020. Mapping of Surface Deformation and Displacement Associated with the
778 6.5 Magnitude Botswana Earthquake of 3 April 2017 Using DInSAR Analysis,
779 Geomat. Environ. Eng., 14, 4, https://doi.org/10.7494/geom.2020.14.4.81
780 Utsu T., Ogata, Y., Matsu'ura ; R.S., 1995. The centenary of the Omori formula for a decay
781 law of aftershock activity, J. Phys. Earth, 43, 1-33.

782 Waldhauser, F., Ellsworth, W. L., 2000. A Double-Difference Earthquake Location
783 Algorithm: Method and Application to the Northern Hayward Fault, California, Bull.
784 Seismol. Soc. Am., 90 (6), 1353 – 1368.
785 Waldhauser, F., 2001. HypoDD: A computer program to compute double-difference
786 earthquake locations, USGS Open File Rep., 01-113.
787 Wessel, P., Smith, H.F., 1998. New, improved version of the generic mapping tools released.
788 EOS Trans. AGU 79, 579.
789 Williamson, I. T., 1996. The geology of the areas around Mmamabula and Dibete: including
790 an account of the Greater Mmamabula Coalfield, Geological Survey Department:
791 District Memoir 6, Chapter 1, pp 03.
792 Zoback, M. L., Zoback, M. D., 1989. Tectonic stress field of the continental United States: In
793 Geological Society of America Memoir 172, Chapter 24, 523 – 539.
794

795 # Tables

Seismological Centre	Long. (°)	Lat. (°)	M_0 (Nm)	M_w	Depth (km)	Strike	Dip	Rake
USGS (Wpha)	25.15	-22.678	$6.19\ 10^{18}$	6.5	23.5	343	44	-62
GFZ	25.22	-22.66	$6.3\ 10^{18}$	6.5	27	331	37	-73
Geoscope	25.15	-22.678	$5.86\ 10^{18}$	6.4	29	333	36	-72
CMT Harvard	25.21	-22.54	$7.01\ 10^{18}$	6.5	30	332	41	-70
CGS (Pretoria) Midzi et al. (2018)	25.134	-22.565	-	6.5	26.5 ±2.5	340	46	-61
This study (InSAR)	25.134	-22.565	$3.68\ 10^{18}$	6.4	22 ±1.5	315	45	-80

796

797 ***Table 3**: Source parameters of the 3 April 2017 earthquake.*

798

Modified depth to top of layer (km)	P-wave velocity (km/s)
0.00	5.80
20.00	6.50

38.00	8.04

***Table 2**: Velocity model (Midzi et al., 2010) used in initial location of aftershocks using Seisan software as well as in the double difference relocation using the hypoDD software.*

Table Captions

Table 4: Source parameters of the 3 April 2017 earthquake.

Table 2: Velocity model (Midzi et al., 2010) used in initial location of aftershocks using Seisan software as well as in the double difference relocation using the hypoDD software.

Resources

- Topography GEBCO: https://www.gebco.net/data_and_products/gridded_bathymetry_data/
- Topography SRTM 3" and 1": https://topex.ucsd.edu/gmtsar/demgen/
- Database of the Seismotectonic Map of Africa: Meghraoui et al., 2016
- ESA Sentinel images : https://sentinel.esa.int/web/sentinel/sentinel-data-access
- SEISAN package : ftp://ftp.geo.uib.no/pub/seismo/SOFTWARE/SEISAN/
- HypoDD: https://www.ldeo.columbia.edu/~felixw/hypoDD.html
- WinTensor software: http://damiendelvaux.be/Tensor/WinTensor/win-tensor_download.html